

Core dynamics of a strained vortex: instability and transition

By D. S. PRADEEP AND F. HUSSAIN

Department of Mechanical Engineering, University of Houston, Houston, TX, 77204-4006, USA

(Received 27 July 2000 and in revised form 29 May 2001)

We study the instability of a laminar vortex column (in an external orthogonal strain field) to an axisymmetric core size perturbation, and the resulting transition to fine-scale turbulence. The perturbation, which evolves as a standing wave oscillation (i.e. *core dynamics*, CD), is inviscidly amplified by the external strain. Analysis of a weakly strained Rankine vortex explains the physical mechanism of instability: resonant interaction between the perturbation – the azimuthal wavenumber $m = 0$ wave – and $m = \pm 2$ waves. The CD instability (CDI) – a type of elliptic instability – experiences the fastest growth when the CD oscillation frequency equals vortex column's fluid angular velocity, such matching occurring only at specific discrete values of the axial wavenumber k . At this resonant frequency, the net effect of the swirl-induced tilting of perturbation vorticity and the CD-induced tilting of base flow vorticity is such that perturbation vorticity is continually aligned with the stretching direction of the external strain. Such strain–vorticity locking occurs for all m ; hence all waves are unstable, the instability oscillation frequency being dependent on m . In a viscous Gaussian-like vortex, CDI has low-strain, low- Re and high- k cutoffs – consequences of the competing effects of inviscid amplification and viscous damping. Direct numerical simulation reveals two physical-space mechanisms of transition: (i) formation of a thin annular vortex sheath surrounding a low-enstrophy ‘bubble’ (similar to axisymmetric vortex breakdown) and the sheath's subsequent roll-up into smaller ‘vortexlets’; and (ii) folding and reconnection of core vortex filaments giving rise to additional fine-grained random vorticity within the bubble – both mechanisms caused by CD-induced intense axial flow within the vortex column. The resulting finer tubular vortices (similar to ‘worms’) have in turn their own CD, and thus this transition scenario suggests a physical-space cascade process in developed turbulence (as well as a concomitant anti-cascade process during the bubble's collapse phase). Additionally, we show that bending waves, in spite of their faster growth, effect surprisingly much slower transfer of energy into fine scales than CDI does, and hence are less effective than CDI in vortex transition and in turbulence cascade.

1. Introduction

The effect of an external non-axisymmetric strain on a vortex is known to be destabilizing, the research focus so far having been on modes that bend the vortex axis, i.e. on bending waves, BW (see, e.g., Eloy & Le Dizès 1999; Leblanc & Cambon 1998; Robinson & Saffman 1984). In this paper, we focus on how the strain also promotes the growth of *axial* waves (may alternatively be called ‘bulging’ or ‘varicose’ waves), i.e. perturbations that cause core vorticity variation without deflecting the vortex axis. Our study is motivated by the observation that coherent structures (vortices)

in turbulence have non-trivial axial structure, such as non-uniform core area, axial inhomogeneity of core vorticity distribution, and helical vortex lines. These features are of course coupled: helical vortex lines induce axial flow that stretches/compresses core vorticity; and, vice versa, non-uniformity of core vorticity (or core area) causes vortex lines to become coiled due to the axial variation of swirl; and so on. ‘Core dynamics’ (CD), i.e. the evolution of a vortex due to its internal, or core, vorticity distribution – distinct from the self-induced motion of the vortex due to non-rectilinearity of its axis often studied by the local induction approximation (Batchelor 1967) – is prevalent in many flows. During vortex reconnection, filaments containing reconnected vorticity (i.e. bridges) reveal CD (Melander & Hussain 1988). Vortices undergoing the typical localized pairing (such as helical pairing in a mixing layer) together behave like a single structure with a large core variation and evolve via CD (Schoppa, Hussain & Metcalfe 1995). A vortex subjected to non-uniform axial stretching develops core-area-varying waves (Verzicco, Jiménez & Orlandi 1995; Marshall 1997). Intense fine-scale vortices in isotropic turbulence (the so-called ‘worms’), whose radii are typically $\simeq \eta$ (Kolmogorov lengthscale) and whose lengths are $\simeq \lambda$ (Taylor microscale) (e.g. Vincent & Meneguzzi 1994; Jiménez & Wray 1998), unavoidably have CD because of their limited axial length. Simulation of an isolated finite-length vortex by Samuels (1998) revealed coiling of vortex lines and hence axial flow – a simple consequence of CD – which he termed ‘instability’, although the CD in this case involves no instability.

Motivated by the vortex breakdown phenomenon, a number of studies have addressed axisymmetric waves on an isolated vortex column, usually with axial flow (see, e.g., Lundgren & Ashurst 1989; Leibovich & Kribus 1990). Leonard (1994) developed a theory of nonlinear axisymmetric waves based on the coupling between core area variation and meridional flow, and showed that very large core area variations can develop in the presence of axial flow. This paper, which expounds Pradeep (1999) and Hussain (1998), considers CD in a vortex without axial flow.

Melander & Hussain (1994, hereinafter cited as MH) studied an isolated vortex column, without axial flow, that initially has sinusoidally varying core size. The immediate CD-induced coiling of vortex lines makes the perturbation evolve as a standing wave driven by the mutual coupling of differential angular velocity along a vortex line and self-induced meridional flow, i.e. radial and axial velocity components u_r and u_z (discussed in §2.2). CD involves no instability in the absence of external strain and is sustained indefinitely in the inviscid limit. In a viscous flow, CD is damped. The oscillation frequency increases as the vortex Reynolds number ($Re \equiv \text{circulation}/\text{viscosity}$) is increased, with a finite inviscid limit. CD is thus a specific case of waves on a vortex column known since Kelvin (Kelvin 1880; Saffman 1992). (For a recent study of Kelvin vortex waves, see Arendt, Fritts & Andreassen 1997.) These waves, identified by azimuthal wavenumber m , include both bending and axial waves: $m = 1$ and $m = -1$ are bending waves, while waves of all other m do not deflect the vortex axis and are therefore axial waves. (The MH flow corresponds to the nonlinear $m = 0$ wave.) All Kelvin vortex waves are neutrally stable in an inviscid flow.

A vortex segment in turbulence is not of course isolated, but is advected and strained by the induced velocity of adjacent vortex filaments. A first approximation of the external effect is uniform plane strain orthogonal to the vortex, which deforms the vortex core into an elliptic shape (Kida 1981; Moffatt, Kida & Ohkitani 1994; Jiménez, Moffatt & Vasco 1996). The elliptic vortex is unstable to three-dimensional perturbations, as shown by Moore & Saffman (1975) and Tsai & Widnall (1976). To understand the growth of BW on a vortex ring, Tsai & Widnall considered a weakly strained Rankine vortex column perturbed with $m = 1$ and $m = -1$ waves,

both having the same axial wavenumber k . The π -periodic strain couples m with $m \pm 2$ waves (S. Le Dizès 1999, personal communication). For $m = \pm 1$, Tsai & Widnall found that for certain discrete values of k at which the oscillation frequency of both modes is zero, there is resonant amplification (i.e. instability). Finite strain broadens the discrete k values at which instability occurs, the bandwidths increasing with increasing strain (Robinson & Saffman 1984).

Pierrehumbert (1986) analysed elliptic vortex instability in an unbounded flow formed by the superposition of uniform strain and uniform vorticity. Bayly (1986) developed a theory of the ‘elliptic instability’ in terms of waves of the form $\mathbf{u}' = \mathbf{u}(t) \exp[i\mathbf{k}(t) \cdot \mathbf{x}]$ that are supported by a flow in solid-body rotation, where \mathbf{k} is inclined at angle α to the vortex axis. The perturbation rotates about the wavevector \mathbf{k} with a frequency $\Omega \cos \alpha$, where Ω is the base flow vorticity. In the limit of vanishing strain rate, \mathbf{k} itself rotates about the vortex axis with the frequency $\Omega/2$ in the direction opposite to that of the perturbation. The two rotations, therefore, cancel when $\alpha = 60^\circ$; an infinitesimal strain then causes exponential perturbation growth by stretching (Waleffe 1990). The range of α for which instability occurs increases with increasing strain rate. Waleffe recovered the Kelvin wave eigenmodes by superposing rotating Fourier modes, linking the Kelvin wave and elliptic instability analyses. The elliptic instability can be interpreted as the ultra-short-wave Kelvin wave instability (Saffman 1992).

The elliptic instability is generic to strained vortices: Stuart vortex (Stuart 1967; Pierrehumbert & Widnall 1982); two-dimensional Taylor–Green vortex (Sipp & Jacquin 1998; Lundgren & Mansour 1996), Stuart and Taylor–Green vortices with system rotation (Leblanc & Cambon 1998; Sipp, Lauga & Jacquin 1999); Lamb–Oseen vortex (Eloy & Le Dizès 1999); vortex dipoles (Leweke & Williamson 1998; Billant, Brancher & Chomaz 1999); and Burgers vortex in an additional non-axisymmetric strain (Eloy & Le Dizès 1999). Pierrehumbert (1986) proposed elliptic instability as a fundamental cascade mechanism because the instability’s broadband (in k) growth behaviour implies that a wide range of scales (limited only by viscous cutoff) can simultaneously appear once an elliptic eddy is formed, for example, via Kelvin–Helmholtz roll-up of a shear layer. This cascade hypothesis is supported by the experiments of Malkus (1989). In their simulation of a vortex in a rectangular box, Lundgren & Mansour (1996) introduced simultaneous three-dimensional perturbations (Fourier modes) over a range of k values, and observed transition to a turbulent flow containing fine-scale vortices. While their visualizations show a BW to be the dominant feature of the flow, vortex core variations (i.e. CD) are also evident, but not explored.

So far, most studies of strained vortex instability have focused on the BW, which in general is the most unstable mode of an inhomogeneous vortex. Herein, we focus on the instability triggered by an axisymmetric core-area-varying perturbation, i.e. CD *instability* (CDI). We find that CDI occurs via the resonant growth of $m = 0$ and ± 2 waves, analogous to the growth of superposition of $m = \pm 1$ waves in the case of BW. BW and CDI are both particular types of elliptic instability. CDI has been observed before—in the Stuart vortex (Schoppa *et al.* 1995) and in a vortex dipole (Billant *et al.* 1999)[†]. Despite its weaker growth in practical vortices, CDI can be dominant in a number of flows. For example, intense CDI, triggered in a mixing layer via helical pairing of spanwise rolls, causes transition more rapidly than other mechanisms (Schoppa *et al.* 1995). CDI is likely in worms, which are subjected to

[†] A referee brought to our attention that Gledzer & Ponomerev (1992) analysed the linear stability of both CDI and BW in an elliptic cylindrical container, and that Mason & Kerswell (1999) performed weakly nonlinear analysis of the two instabilities.

simultaneous axial stretching and compression (Jiménez & Wray 1998); modelling a worm by an axisymmetric vortex placed in a non-uniform (zero-mean) axial strain, Verzicco & Jiménez (1999) showed that the vortex survives local compression (by the imposed strain) by developing large-amplitude core area variations. An additional plane strain, typical for worms, is likely to cause instability at large Taylor microscale Reynolds numbers (Re_λ). Waves are triggered on a coherent vortex column via its interaction with ambient fine-scale turbulence (Miyazaki & Hunt 2000). Melander & Hussain (1993a) showed that the vortex column organizes the surrounding fine-scale turbulence into polarized (right- or left-handed vorticity) ‘threads’ that wrap around the vortex; like-handed threads pair to form larger ring-like structures in an antiscascade process. An idealization of such a flow, namely a vortex surrounded by rings of alternating sign, was studied by Marshall (1997), who found that the column develops core-area-varying waves.

Our objective is to understand linear and nonlinear CDI in a simple flow. We first analyse CDI in a weakly strained Rankine vortex (§2). The focus is on the physical interpretation of instability in terms of how sustained stretching occurs at resonance between $m = 0$ and $m = \pm 2$ waves. This physical mechanism is seen also to operate for more complex waves (i.e. those with larger $|m|$). The effect of viscosity and large strain on linear stability is then studied in a Gaussian-like vortex (§3). In §4, nonlinear CDI evolution (obtained via direct numerical simulation, DNS) is shown to result in transition to turbulence via the formation of numerous tubular vortices, and the physical-space mechanisms of transition are identified. We then compare nonlinear CDI and BW evolutions (§5), and discuss the unexpected result that fine-scale turbulence generation is more rapid for CDI. Concluding remarks appear in §6.

2. Linear CDI of an (inviscid) Rankine vortex

2.1. Stability analysis

We consider an axisymmetric Rankine vortex column of uniform vorticity Ω_0 and core radius R_0 . It is well known that the vortex supports small-amplitude three-dimensional waves. In cylindrical polar coordinates (r, θ, z) , these waves have the form,

$$f = \tilde{f}(r)e^{ikz+im\theta+\sigma t} + \text{c.c.}, \quad (2.1)$$

where f is any perturbation quantity (velocity, pressure, etc.), with k being the axial wavenumber, m the azimuthal wavenumber (which is of course an integer), and $\sigma = \sigma_r + i\sigma_i$, σ_r being the growth rate and σ_i the wave oscillation frequency; ‘c.c.’ denotes the complex conjugate. All waves (2.1) are neutrally stable ($\sigma_r = 0$) on an isolated vortex (see Saffman 1992).

Superimposing on the vortex a weak irrotational stagnation-point flow,

$$U_r(r, \theta) = -\epsilon^* r \sin 2\theta, \quad U_\theta(r, \theta) = -\epsilon^* r \cos 2\theta, \quad U_z = 0,$$

yields the base flow:

$$\left. \begin{aligned} U_r(r, \theta) &= -\epsilon r \sin 2\theta + O(\epsilon^2), \\ U_\theta(r, \theta) &= r - \epsilon r \cos 2\theta + O(\epsilon^2), \\ P(r, \theta) &= r^2/2 - 1 + O(\epsilon^2), \end{aligned} \right\} \quad r \leq R(\theta), \quad (2.2)$$

$$\Phi = \theta - \frac{1}{4}\epsilon(r^2 - r^{-2}) \sin 2\theta + O(\epsilon^2), \quad r \geq R(\theta),$$

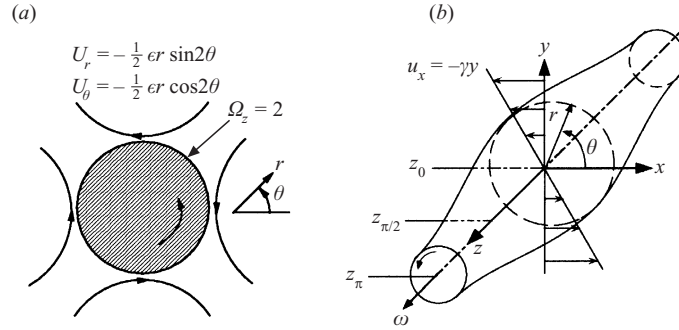


FIGURE 1. Schematics of base flows. (a) A Rankine vortex in weak irrotational strain. (b) A Gaussian-like vortex with sinusoidal core perturbation in plane shear.

where the scaled strain rate $\epsilon (\equiv 4\epsilon^*/\Omega_0) \ll 1$, P is pressure, and Φ is the velocity potential of the irrotational flow outside the vortex core. Here, we have scaled the velocities by $\Omega_0 R_0/2$ and the velocity potential by $\Omega_0 R_0^2/2$, with R_0 as the lengthscale and $2/\Omega_0$ the timescale. $R(\theta)$ represents the elliptic vortex core boundary. The ellipse major and minor axes are inclined at 45° to the strain's principal axes, which are along the lines $\theta = \pi/4, -3\pi/4$ (compression) and $\theta = 3\pi/4, -\pi/4$ (stretching). The base flow (2.2) is sketched in figure 1(a), with the scaled quantities and the coordinate system indicated.

We subject the flow to a small-amplitude three-dimensional perturbation, which is expanded as a perturbation series in ϵ :

$$f = \sum_m [(f_m^{(0)} + \epsilon f_m^{(1)})e^{ikz+im\theta+(\sigma_m^{(0)}+\epsilon\sigma_m^{(1)})t}] + \text{c.c.} + O(\epsilon^2). \quad (2.3)$$

By inserting (2.3) into the linearized governing equations, one obtains an hierarchy of eigenvalue problems. The boundary conditions are that the core boundary is a material surface and that pressure is continuous across this boundary. In addition, the perturbation is required to be non-singular at $r = 0$ and as $r \rightarrow \infty$.

Axisymmetric core perturbation. Because of the strain, an axisymmetric core perturbation ceases to be axisymmetric, i.e. the $m = 0$ perturbation generates $m = 2$ and $m = -2$ waves. To solve for the CDI eigenmode, we need to consider a perturbation that has $m = 0, \pm 2$ azimuthal components in (2.3). In fact, only one of $m = +2$ and $m = -2$ is required because of two symmetry properties of the governing equations. The first (conjugate) symmetry,

$$f_{-m}^{(j)}(-k) = f_m^{(j)*}(k), \quad \sigma_{-m}^{(j)}(-k) = \sigma_m^{(j)*}(k) \quad (2.4)$$

(where $*$ denotes complex conjugation) is the consequence of the base flow being real. The second symmetry is obtained by changing the sign of k but not of m . Then,

$$f_m^{(j)}(-k) = f_m^{(j)}(k), \quad (2.5a)$$

$$u_{z,m}^{(j)}(-k) = -u_{z,m}^{(j)}(k), \quad (2.5b)$$

$$\sigma_m^{(j)}(-k) = \sigma_m^{(j)}(k). \quad (2.5c)$$

Here, $f_m^{(j)}$ represents radial or azimuthal velocity, or pressure or velocity potential; $u_{z,m}^{(j)}$ is the axial velocity component u_z of the m -mode. Note that the second symmetry (2.5) implies a change in the sign of m/k and hence a change from a right-handed helical perturbation to a left-handed one, or vice versa. Further, since the sign of the

axial phase velocity $\text{Im}\{\sigma_m^{(j)}\}/k$ is reversed, the left-handed and right-handed waves travel in opposite directions along the vortex axis and with the same speed. Using (2.4) and (2.5), the eigenmode for the case of resonance between $m = 0$ and -2 can be recovered from the eigenmode of the $m = 0, 2$ case. We therefore focus on the $m = 0, 2$ case in the following.

$O(\epsilon^0)$ solution. At $O(\epsilon^0)$, the $m = 0$ and $m = 2$ waves evolve independently, and the oscillation frequencies $\sigma_m^{(0)}$ satisfy the well-known dispersion relation (§12.1 of Saffman (1992)),

$$kK'_m(k)J_m(\eta_m) + (\sigma_m^{(0)} + im)K_m(k)\mathcal{A}_m = 0, \quad m = 0, 2, \quad (2.6)$$

where

$$\eta_m^2 \equiv -\frac{k^2(\sigma_m^{(0)} + i2 + im)(\sigma_m^{(0)} - i2 + im)}{(\sigma_m^{(0)} + im)^2}, \quad (2.7a)$$

and

$$\mathcal{A}_m \equiv -\frac{(\sigma_m^{(0)} + im)dJ_m(\eta_m r)/dr|_{r=1} + 2imJ_m(\eta_m)}{(\sigma_m^{(0)} + i2 + im)(\sigma_m^{(0)} - i2 + im)}. \quad (2.7b)$$

Here J_m and K_m are the Bessel and modified Bessel functions of order m respectively. Salient features of the eigenvalues $\sigma_m^{(0)}$ are reviewed below.

At any k value, there is an infinite number of discrete $\sigma_m^{(0)}$ that satisfy (2.6). All $\sigma_m^{(0)}$ are imaginary and are bounded, with

$$-i(2 + m) < \sigma_m^{(0)} < i(2 - m). \quad (2.8)$$

Eigenvalues $\sigma_m^{(0)}$ occur in pairs, both associated with the same η_m^2 value: there is one $\sigma_m^{(0)}$ corresponding to $+(\eta_m^2 + k^2)^{1/2}$ and another corresponding to $-(\eta_m^2 + k^2)^{1/2}$. As k increases, the $\sigma_m^{(0)}$ approach the upper bound in (2.8) for $+(\eta_m^2 + k^2)^{1/2}$ and the lower bound for $-(\eta_m^2 + k^2)^{1/2}$. The eigenvalues with the smallest η_m^2 are the closest to the bounds at any given k . As η_m^2 increases, so does the number of radial oscillations in the eigenmode. We pursue here the simpler modes, i.e. those with the lowest few η_m^2 values. The first few eigenvalues $\sigma_m^{(0)}(k)$ for $m = 0, \pm 2$ are plotted in figure 2, where some interesting ‘crossing-points’ are identified by $+$ and \times symbols.

The $m = 0$ and $m = 2$ waves have different oscillation frequencies, i.e. $\sigma_0^{(0)}(k) \neq \sigma_2^{(0)}(k)$, except at specific discrete values of k at which the purely imaginary eigenvalues $\sigma_0^{(0)} = \sigma_2^{(0)} (\equiv \sigma^{(0)})$, e.g. points in figure 2 identified by $+$ marks. At the crossing-points, resonance between $m = 0$ and $m = 2$ waves can lead to perturbation growth in the presence of an external strain. That is, the $m = 0$ wave interacts with the base flow to force the $m = 2$ wave, and vice versa. As this forcing has the same frequency as the wave oscillation, resonant growth of wave amplitude is possible. We now explore the instability at the crossing-points.

$O(\epsilon^1)$ solution. The $O(\epsilon^1)$ eigenvalue problem is solved analytically following Tsai & Widnall (1976). Only the results are discussed here, and some details of the solution are given in Appendix A.

Briefly, manipulation of the governing equations yields a single equation for the pressure perturbation $p_m^{(1)}$. This equation for pressure and the potential-flow equation are solved, and the boundary conditions at the core edge are enforced. This procedure yields a linear inhomogeneous system involving $\sigma_m^{(1)}$ and the unknown amplitudes of $p_m^{(1)}$ and $\phi_m^{(1)}$. The solution of the linear system must satisfy a solvability condition, which is the expression for $\sigma_m^{(1)}$. One finds that for wave amplification to occur, $\sigma_0^{(1)} = \sigma_2^{(1)} (\equiv \sigma^{(1)})$.

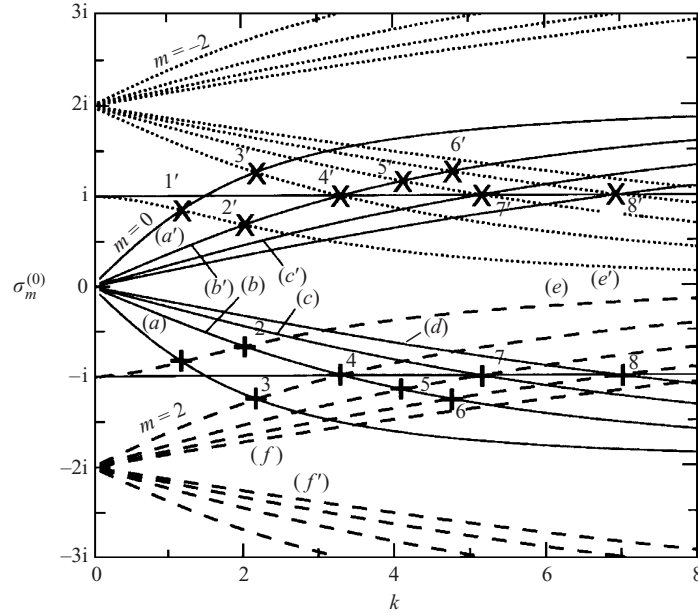


FIGURE 2. Oscillation frequency $\sigma_i \equiv \text{Im}\{\sigma_m^{(0)}\}$ vs. axial wavenumber k for $m = 0$ (solid lines), $m = 2$ (dashed lines) and $m = -2$ (dotted lines); $+$ denotes $m = 0, 2$ crossing-points. Growth rates $\text{Re}\{\sigma^{(1)}\}$ at $+$ points appear in table 1; \times denotes $m = 0, -2$ crossing-points. Note that curves $(a'-d')$ are for progressively increasing $+(\eta_m^2 + k^2)^{1/2}$ and curves $(a-d)$ are the sister curves, i.e. for progressively decreasing $-(\eta_m^2 + k^2)^{1/2}$. There is an infinity of curves between (d) and (d') for $m = 0$ (not shown), as also between (f) and (f') for $m = 2$ case. Among all the curves in the range $-2i < \sigma_m^{(0)} < 0$, curves (a) and (e) are the only ones without a crossing-point at $\sigma^{(0)} = -i$.

Crossing point	k	$\sigma^{(0)}$	$\sigma^{(1)}$
4	3.3093	$-0.9962i$	0.5376
7	5.1723	$-1.0027i$	0.5678
8	7.0228	$-1.0036i$	0.5666
1	1.1927	$-0.8425i$	0.4627
6	4.7662	$-1.2614i$	0.1375
5	4.1230	$-1.1561i$	0.1171
2	2.0651	$-0.6731i$	0.0898
3	2.1904	$-1.2571i$	0.0997

TABLE 1. CDI wavenumber k , oscillation frequency $\sigma^{(0)}$ and growth rate $\sigma^{(1)}$ for $+$ points in figure 2, listed in order of decreasing growth rate.

The growth rate $\sigma^{(1)}$ has been computed for the $+$ points in figure 2 and is given in table 1. At all $+$ points, $\sigma^{(1)}$ is real and positive, i.e. instability occurs at all these points; the growth rate however is not the same at all points. A striking feature is that the largest growth occurs whenever $\sigma^{(0)} \simeq -i$ (i.e. $+$ points 4, 7 and 8 in figure 2). This growth rate is the same irrespective of k . Recall that the angular velocity is scaled by $2/\Omega_0$. Thus, $\sigma^{(0)} = -i$ implies that the *CD oscillation frequency equals the vortex column's fluid angular velocity*. This frequency condition for maximum growth is discussed in the following subsection (§ 2.2).

The peak CDI growth rate value (at $+$ point 7) of 0.5678ϵ nearly equals the value

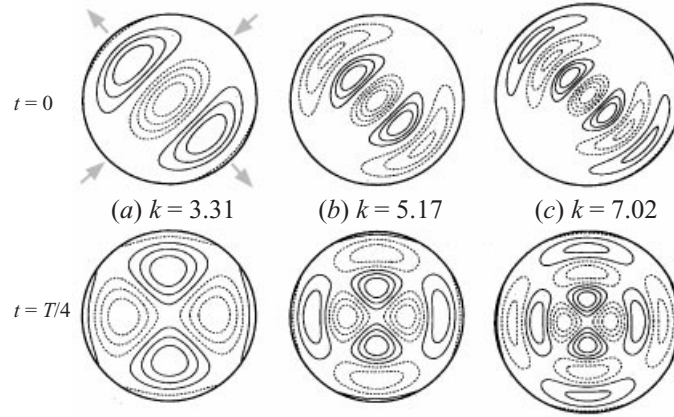


FIGURE 3. ω_z contours in the z_0 plane for modes with maximum growth (+, points 4, 7 and 8 in figure 2) with k values indicated. Eigenmodes are shown at two phases of the oscillation. Dashed contours indicate $-\omega_z$. Arrows outside the circular core denote strain principal axes.

obtained for BW by Tsai & Widnall (1976) of 0.57ϵ . (For an unbounded elliptic vortex, Waleffe (1990) found that instability growth rate has an upper bound of 0.5625ϵ . As the perturbation is increasingly localized near the axis with increasing k , the $k \rightarrow \infty$ limit in our flow corresponds to a vortex of infinite core size. With increasing k , we find that the growth rate does asymptote to 0.5625ϵ , decreasing from 0.5678ϵ at $k = 5.17$ to 0.5625ϵ for $k \geq 525.78$.) The equal growth of CDI and BW instabilities is a feature contrary to that of vortices with inhomogeneous core vorticity profiles. For example, in the Stuart vortex, CDI has approximately half the growth rate of BW instability (Pierrehumbert & Widnall 1982; Schoppa *et al.* 1995) – BW being the most unstable mode and CDI the second most unstable mode. We find similar weaker CDI growth in a Gaussian-like vortex (§3.2), and discuss there the possible reason for this difference between Rankine and inhomogeneous vortices. Figure 3 shows the axial vorticity perturbation ω_z distributions of the fastest growing eigenmodes, at $k = 3.31$, 5.17 and 7.02 (+ points 4, 7 and 8 respectively in figure 2). Since the eigenmodes are oscillatory, the ω_z distribution in any z -plane is different at different phases of the oscillation. Figure 3 shows the eigenmodes at two (opposite) phases: $t = 0$ (top row) and $t = T/4$ (bottom row), where T is the oscillation time period. As k increases, the number of nodes in the radial profile of ω_z increases. Also, as expected, regions of higher perturbation vorticity (ω_z) are progressively confined closer to the axis. This feature is also true of other components of perturbation vorticity (not shown).

Note that there is an infinite number of crossing-points where $\sigma^{(0)} = -i$, and that there are such crossing-points even as $k \rightarrow \infty$. Since the growth rate 0.57ϵ seems to be independent of k , we expect that all waves with $\sigma^{(0)} = -i$ amplify equally. This short-wave nature of the instability, combined with the increasing localization of perturbation near the axis with increasing k , suggests that CDI should be insensitive to the curvature of the vortex axis. CDI should thus occur even in vortices whose axes are curved, such as vortex rings.

Standing wave oscillation. The eigenmodes due to the superposition of $m = 0$ and $m = 2$ waves (+ points in figure 2) travel in the $+z$ -direction as the axial phase velocity $\text{Im}\{\sigma^{(0)}\}/k < 0$. The corresponding CDI eigenmodes due to superposition of $m = 0$ and $m = -2$ waves (\times points) travel in the $-z$ -direction, with axial phase velocity $\text{Im}\{\sigma^{(0)}\}/k > 0$. (Note that crossing-points 1 and $1'$, 2 and $2'$, etc. have the

same k .) Both eigenmodes have the same oscillation frequency and growth rate—a consequence of (2.4) and (2.5). As an axisymmetric core size perturbation triggers both eigenmodes, a standing wave oscillation emerges. The vortex dynamics of this standing wave are discussed below.

2.2. Physical interpretation of instability

To understand the frequency condition for maximum growth, we focus on the eigenmode vortex dynamics, amenable to interpretation in terms of vortex tilting and stretching. We first consider CD in the absence of any external strain. The perturbation evolves as a periodic expansion and contraction of core size, and hence coiling, uncoiling, and then reverse coiling of vortex lines. The evolution of perturbation vorticity during this oscillation explains why the instability occurs when the CD frequency equals the fluid angular velocity.

CD oscillation with no strain. An axisymmetric perturbation to the Rankine vortex satisfies the linearized vorticity equation

$$\frac{D}{Dt} \begin{pmatrix} \omega_r \\ \omega_\theta \\ \omega_z \end{pmatrix} = \underbrace{\begin{pmatrix} -\omega_\theta \\ \omega_r \\ 0 \end{pmatrix}}_{\text{T1}} + 2 \underbrace{\frac{\partial}{\partial z} \begin{pmatrix} u_r \\ u_\theta \\ u_z \end{pmatrix}}_{\text{T2}}, \quad (2.9)$$

where $D/Dt \equiv \partial/\partial t + \mathbf{U} \cdot \nabla$; the lower-case quantities correspond to the perturbation. Here we have used the scaled velocity and vorticity values. Recall that our timescale is $2/\Omega_0$; therefore, base-flow vorticity magnitude equals 2, and angular velocity U_θ/r ($= \partial U_\theta/\partial r$, for the Rankine vortex) equals 1.

The first term on the right-hand side in (2.9) (call it T1) describes the tilting by the vortex swirl of ω_r into ω_θ , and vice versa. Let $\boldsymbol{\omega}_\perp$ denote the the perturbation vorticity vector in an axial plane (perpendicular to the z -direction), i.e. $\boldsymbol{\omega}_\perp \equiv (\omega_r, \omega_\theta)$. We can see from (2.9) that T1 rotates $\boldsymbol{\omega}_\perp$ in the $+\theta$ -direction. More precisely, this rotation has the same sense as that of U_θ (which in our coordinate system is along $+\theta$; see figure 1a). The rate at which T1 rotates $\boldsymbol{\omega}_\perp$ equals 1, i.e. it equals the angular velocity of fluid in the vortex.

The second term on the right-hand side in (2.9) (term T2) represents the tilting/stretching of the vortex column's axial vorticity by the gradients of CD-induced perturbation velocity. Since u_r and u_z are induced by ω_θ , and u_θ by ω_r or ω_z , T2 introduces couplings between the various components of perturbation vorticity. These couplings produce the core size oscillation that is CD (MH).

Consider a segment of a vortex tube that is given a sinusoidal axisymmetric core size perturbation (figure 4a) such that all vortex lines are initially uncoiled (i.e. each vortex line lies totally in a meridional plane, i.e. $\omega_\theta = 0$). Since a vortex tube encloses the same circulation $2\pi r(U_\theta + u_\theta)$ at all z , net angular velocity $(U_\theta + u_\theta)/r$ on the tube surface at z_1 (where core radius is reduced) is greater than that at z_2 (where core radius is increased) (figure 4a). It follows that a vortex line passing through fluid particles A in plane z_1 and B in plane z_2 (figure 4a) will immediately thereafter become coiled (figure 4b), since vortex lines are material in an inviscid flow. That is, an $(\omega_r, 0, \omega_z)$ perturbation generates ω_θ , hence both u_z and u_r . The axial flow stretches Ω_z at z_2 and compresses Ω_z at z_1 (via the z -component T2 term in (2.9)). Thus, there is core contraction where the core is expanded (e.g. z_2), and vice versa, causing the core size variation (hence ω_z and ω_r) to be reduced. As the core size variation is being reduced, the vortex lines become increasingly coiled because of the persisting differential swirl

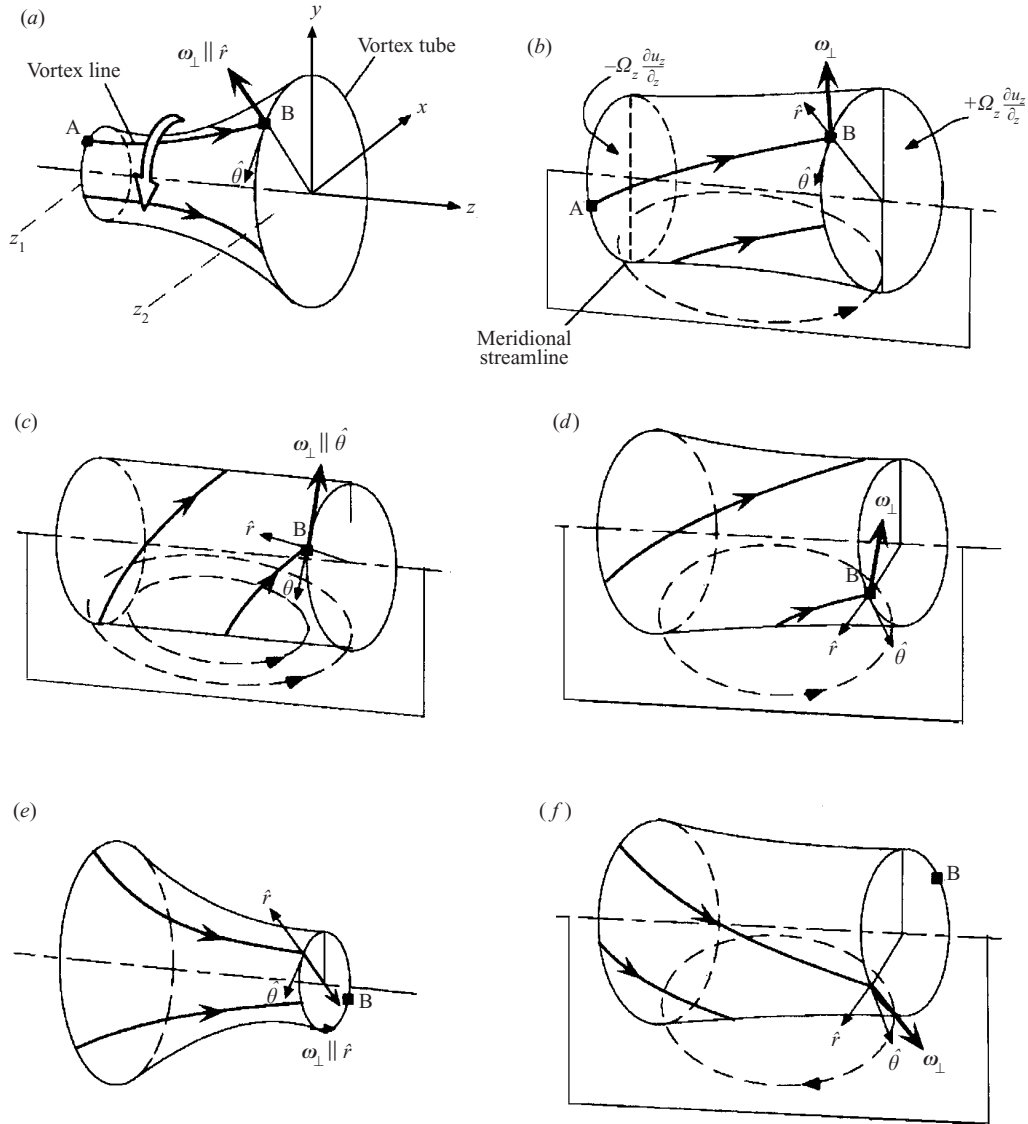


FIGURE 4. Illustration of CD evolution on a vortex tube between planes z_1 and z_2 . Vortex lines lie on an axisymmetric vortex surface. (a) $t = 0$, (b) $T/8$, (c) $T/4$, (d) $3T/8$, (e) $T/2$, (f) $5T/8$.

between A and B, i.e. because $(U_\theta + u_\theta)/r|_A \neq (U_\theta + u_\theta)/r|_B$. Thus, at the instant when the vortex tube becomes cylindrical (figure 4c), vortex lines on the tube surface are coiled. Meridional flow (u_r, u_z) induced by the coiled lines continues to stretch Ω_z at z_2 and to compress Ω_z at z_1 . Thereby, the core size variation begins to reverse from that shown in figure 4(a). Reversal of the core size variation also reverses the sign of the differential swirl, and hence the vortex lines now begin to uncoil (figure 4d). The meridional flow continues to increase the core size variation until the vortex lines are fully uncoiled (figure 4e). At this stage, the core size variation is equal and opposite to that initially (figure 4a). The evolution so far (i.e. from figures 4a to 4e) corresponds to half a cycle of the $m = 0$ standing wave oscillation, which continues indefinitely. (A subsequent stage of the oscillation is shown in figure 4f.)

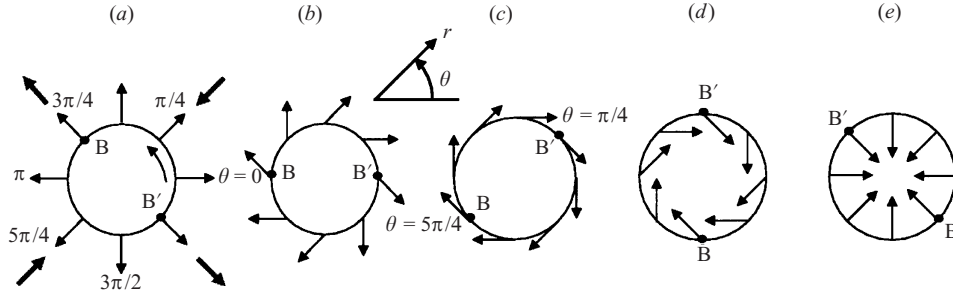


FIGURE 5. Illustration of vorticity locking (in z_2 -plane of figure 4). Among the eight particles shown, only B and B' have strain vorticity locking. Five phases of oscillation (a–e) here correspond to phases (a–e) in figure 4.

For the CD oscillation shown in figure 4, corresponding phases of the ω_\perp evolution in plane z_2 are illustrated in figure 5. The ω_\perp distribution in figure 5 is shown on a circle (within the core); the particles remain on the circle in the limit of infinitesimal perturbation amplitude. Panels (a–e) in figure 5 correspond respectively to the panels (a–e) in figure 4. Notice that during the oscillation, ω_\perp has different orientations at different times, the orientation changing by 180° during half a cycle of the oscillation (panels a–e, figures 4, 5). Now superimpose an infinitesimal uniform strain field on the vortex. Since the strain direction is the same everywhere in the flow and the orientation of ω_\perp changes continually, a fluid particle experiences both vorticity stretching and compression (at different times) due to the external strain. This is true for every fluid particle in the flow. Thus, there need not be any net vorticity amplification and hence no instability.

Strain–vorticity locking. Vorticity amplification will definitely occur if a fluid particle experiences continual stretching. This means that a fluid particle must have ω_\perp perpetually aligned with the strain's stretching direction, i.e. 'strain–vorticity locking'. For ω_\perp of a fluid particle B to be aligned with the strain at all times, B must occupy the azimuthal locations shown in figure 5(a–c). That is, during the evolution from figure 5(a) to figure 5(c), B is advected through an angle of 90° . Since this period corresponds to a quarter-cycle of the CD oscillation, it follows that for strain–vorticity locking to occur the CD oscillation frequency and the fluid angular velocity must be equal. (Could B be advected from (a) to (c) by an additional 360° ? This is not a possibility as the locking will be disrupted in between. Thus, locking can occur only at this unique frequency.) Such alignment locking results in exponential amplification of the fluid's perturbation vorticity.

Because the perturbation is axisymmetric, only certain fluid particles (B and B' in figure 5, which occupy azimuthal locations separated by 180°) experience pure stretching. Also, there are fluid particles whose vorticity always remains along the strain's compressive direction (those initially at $\theta = \pi/4$ and $\theta = 5\pi/4$; figure 5a); perturbation vorticity magnitude of these particles is therefore reduced. Thus, an $m = 0$ perturbation does not remain axisymmetric in the presence of the strain field, but develops an azimuthally π -periodic (i.e. $|m| = 2$) component. The $|m| = 2$ component grows continually from zero amplitude until the amplitudes of $m = 0$ and $|m| = 2$ are *exactly* equal. When this happens, the $|m| = 2$ mode cancels $m = 0$ along the compressive direction; the two modes add along the stretching direction. At locations where $m = 0$ vorticity is aligned with neither the stretching nor the compressive directions of strain, the additive $|m| = 2$ mode 'tilts' $m = 0$ vorticity

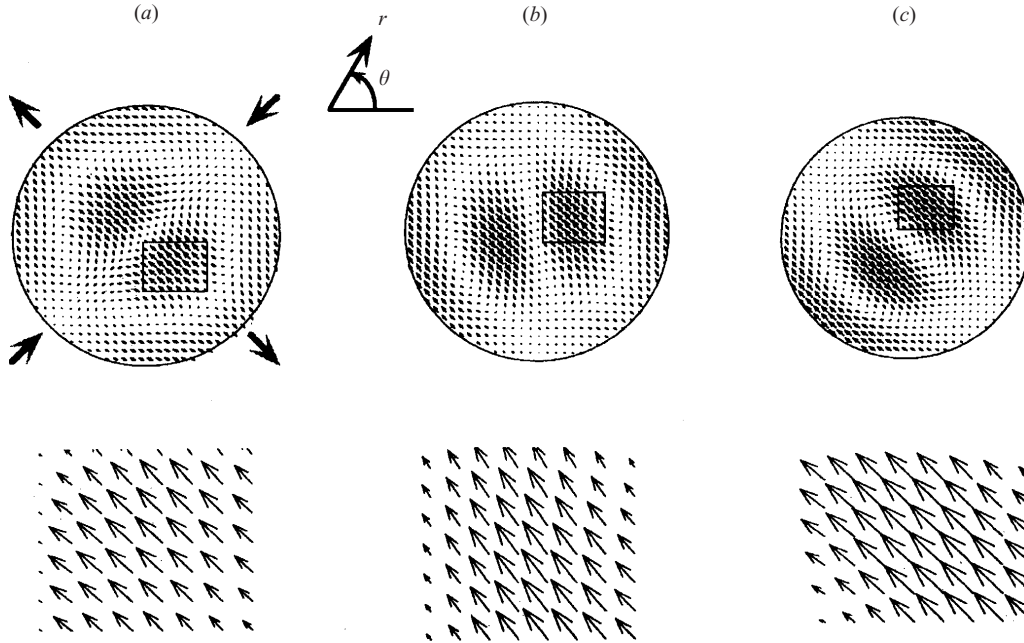


FIGURE 6. Strain-vorticity locking in CDI eigenmode of figure 3(a). ω_{\perp} distribution in $z_{\pi/2}$ (see figure 1b) is shown at three phases of the oscillation: (a) $t = 0$ (maximum core area variation; no vortex line coiling), (b) $t = T/8$ and (c) $t = T/4$ (no core area variation; maximally coiled vortex lines). An expanded view of the square box in the top row is shown underneath.

toward the stretching direction. Thereby, the perturbation evolves such that ω_{\perp} is continually stretched by the external strain.

The analytical solution obtained in §2.1 verifies the above qualitative explanation. Figure 6 shows the ω_{\perp} distribution at three phases of the oscillation: $t = 0$ (maximum core size variation; no vortex line coiling), $t = T/8$ and $t = T/4$ (no core size variation; maximally coiled vortex lines) for the same eigenmode as in figure 3(a). At each phase, there is a patch of fluid (marked by a box in the figure with an expanded view underneath) with ω_{\perp} aligned with the strain. This patch moves in the $+\theta$ -direction from $\theta = \pi/4$ to $\theta = 3\pi/4$ during the time $t = 0$ to $t = T/4$. Note that perturbation vorticity alignment is perfect only at one point, varying by a few degrees within the patches shown. Such strain-vorticity locking is not restricted to particular z -planes but occurs all along the vortex column (shown in Appendix B).

Locking for non-axisymmetric perturbations. It is also shown in Appendix B that locking occurs for resonant combinations of waves other than $m = 0, \pm 2$. The oscillation frequency at which locking occurs depends on m . Locking occurs trivially for BW instability ($m = \pm 1$ waves), as the eigenmode is non-oscillatory (i.e. the perturbation field is steady in the absence of strain). The locking mechanism of growth presented here is consistent with the interpretation of Waleffe (1990) that ‘it is possible to choose initial conditions such that the *average* vorticity is, and *stays*, in the stretching direction’. (His figures 1 and 2 are the BW analogue of our figures 3 and 6.) A strained vortex has therefore a wide variety of unstable modes in addition to CDI and BW[†]. The growth of unstable modes with $|m| > 1$ can explain

[†] Following the submission of this paper, we became aware of an experimental study by Eloy, Le Gal & Le Dizès (2000), in which different Kelvin wave instabilities were realized in a rotating non-axisymmetric cylindrical container.

unusual vortex phenomena, such as the breakup of a vortex into a number of helical filaments, which have been observed in turbulent flows; see, e.g., Cadot, Douady & Couder (1995).

3. CDI of a viscous vortex in shear: linear stability

We next consider linear CDI in a more practical flow, namely a viscous vortex column embedded in an orthogonal shear flow of finite (i.e. non-infinitesimal) strength. A Gaussian-like core vorticity profile is chosen, such a profile being typical of vortices in viscous and turbulent flows. The choice of uniform shear, instead of pure strain, has been dictated by our Fourier pseudospectral DNS algorithm. (Note that a plane shear ($u_x = -\gamma y$) is the superposition of saddle or straining flow ($u_x = -\gamma y/2$, $u_y = -\gamma x/2$) and solid-body rotation ($u_x = -\gamma y/2$, $u_y = \gamma x/2$.) It is the straining component of the shear that is responsible for CDI growth. The essential instability mechanism is unaffected by the vortical component of the shear.

3.1. Base flow

The two-dimensional base flow comprises an axisymmetric vortex column, having a ‘compact Gaussian’ vorticity profile (i.e. a Gaussian-like profile with compact support):

$$\begin{aligned}\Omega_z(\zeta) &= \Omega_0 \exp[-4\zeta^2/(1-\zeta^2) + 4(\zeta^4 + \zeta^6 + \zeta^8)], & \zeta \leq 1 \\ &= 0, & \zeta > 1,\end{aligned}\quad (3.1)$$

where $\zeta \equiv r/r_0$, with $r = (x^2 + y^2)^{1/2}$ and r_0 being the core radius; Ω_0 is the peak vorticity magnitude. Note that Ω_z is continuous and smooth. The vortex column is embedded in a uniform shear flow,

$$U_x(y) = -\gamma y, \quad (3.2)$$

having axial vorticity of the same sign ($+\omega_z$) as the vortex, i.e. the shear strength $\gamma > 0$. This base flow, along with the coordinate system used, is illustrated in figure 1(b).

The CDI growth rate depends on the shear strength γ , the Reynolds number Re , and the perturbation axial wavenumber k . In the following, the relative shear strength, $s \equiv \gamma/\Omega_0$, is varied between 0 and 0.25 by changing the value of γ and keeping Ω_0 fixed ($\Omega_0 = 1$ in all cases); Re (defined below) is varied between 400 and 5000, and k between 0.4 and 2.5. The timescale τ is the eddy turnover time, given by

$$\tau = \pi r_0^2/\Gamma = 4.494/\Omega_0,$$

where Γ is the vortex circulation. The vortex Reynolds number $Re \equiv \Gamma/\nu$, where ν is the kinematic viscosity.

As the strain deforms the vortex into an elliptic shape, the base flow is initially (inviscidly) unsteady, but progressively becomes steady. The L_2 -norm of the difference between flow fields closely separated in time (by $\simeq \tau/10$) is computed, and when the norm drops to a hundredth of its initial value, the flow field is taken to be sufficiently steady for stability analysis. This procedure is repeated for every different s value.

The base flow obtained is illustrated (for $s = 0.1$) in terms of streamlines and vorticity contours in figure 7(a). Note that a two-dimensional flow is inviscidly steady when streamlines and vorticity contours coincide. Figure 7(a) shows such coincidence everywhere in the flow except for small deviations near the core edge, implying that the flow is nearly steady. The vorticity contours are approximately elliptic, and the

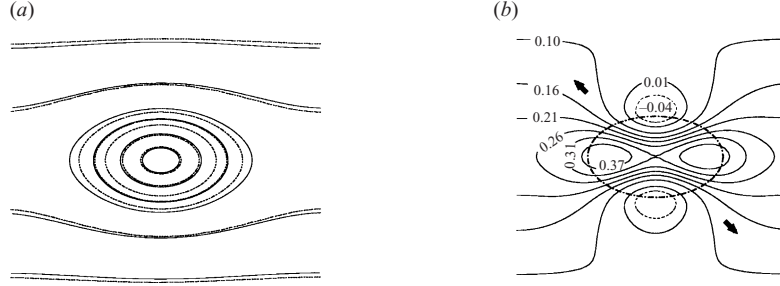


FIGURE 7. (a) Two-dimensional base flow: elliptic Gaussian vortex in uniform shear. Coincidence of $|\Omega_z|$ contours (dotted) and streamlines (solid) implies steadiness. (b) Contours of $S_{ij}\omega_i\omega_j/\omega_k\omega_k$ for only ω aligned with the stretching direction (shown by arrow). Thick dash-dot contour is $\Omega_z = 0.2\Omega_0$.

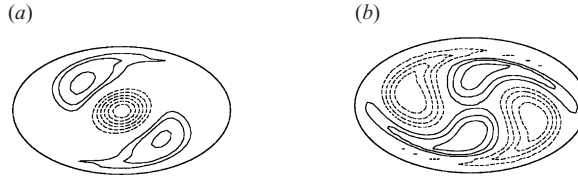


FIGURE 8. ω_z contours (dotted lines denote $-\omega_z$) in the z_π -plane (see figure 1b) for CDI eigenmode shown at two phases: (a) $t = 0$, maximum area variation; no vortex line coiling, (b) $t = T/4$, no area variation; maximum coiling. Outer boundary denotes $\Omega_z = 0.2\Omega_0$ contour. Eigenmode shown for $k = 1$, $s = 0.1$, $Re = 5000$. The outer contours are very close as it is early in the CDI evolution.

major and minor axes of these ellipses are aligned at 45° to the principal axes of the external strain, which lie along lines $y = -x$ (stretching) and $y = x$ (compression). Figure 7(b) shows contours of $S_{ij}\omega_i\omega_j/|\omega|^2$ (where S_{ij} is the strain rate tensor) only for ω along the stretching direction of the external strain. The significance of the radial and azimuthal non-uniformity of this stretching rate is discussed later.

Numerical technique. Details of the Fourier pseudospectral algorithm used to compute the CDI growth rate are given in Appendix C. Briefly, the base flow obtained by the procedure described above is ‘frozen’. The linearized Navier–Stokes equations, initialized with a random three-dimensional perturbation having a single axial wavenumber k , are solved. The perturbation is integrated until the most unstable eigenmodes of the vortex become (energetically) dominant. The fastest growing mode is BW, whose growth rate is twice that of CDI. Time-integration alone therefore does not yield the CDI eigenmode. To obtain this mode, BW and CDI are separated via an orthogonalization-based procedure (Mamun & Tuckerman 1995), which also yields the eigenmode growth rate ($\sigma = \sigma_r + i\sigma_i$). Once an eigenmode has been obtained for a given set of s , k and Re values, the mode is used to initialize subsequent computations in which one or more of these parameters are changed. This procedure reduces the computational effort and also allows an estimate of growth rate cutoffs. When the value of k is changed, the perturbation (i.e. its amplitudes for all (x, y) Fourier modes) is adjusted so as to satisfy the divergence-free condition for vorticity.

3.2. Stability analysis results

CDI eigenmode. The CDI eigenmode (figure 8) is, not too surprisingly, qualitatively similar to that of the Rankine vortex (figure 3). The ω_z perturbation is shown at two phases of the oscillation: $t = 0$ (maximum core area variation; no coiling of vortex

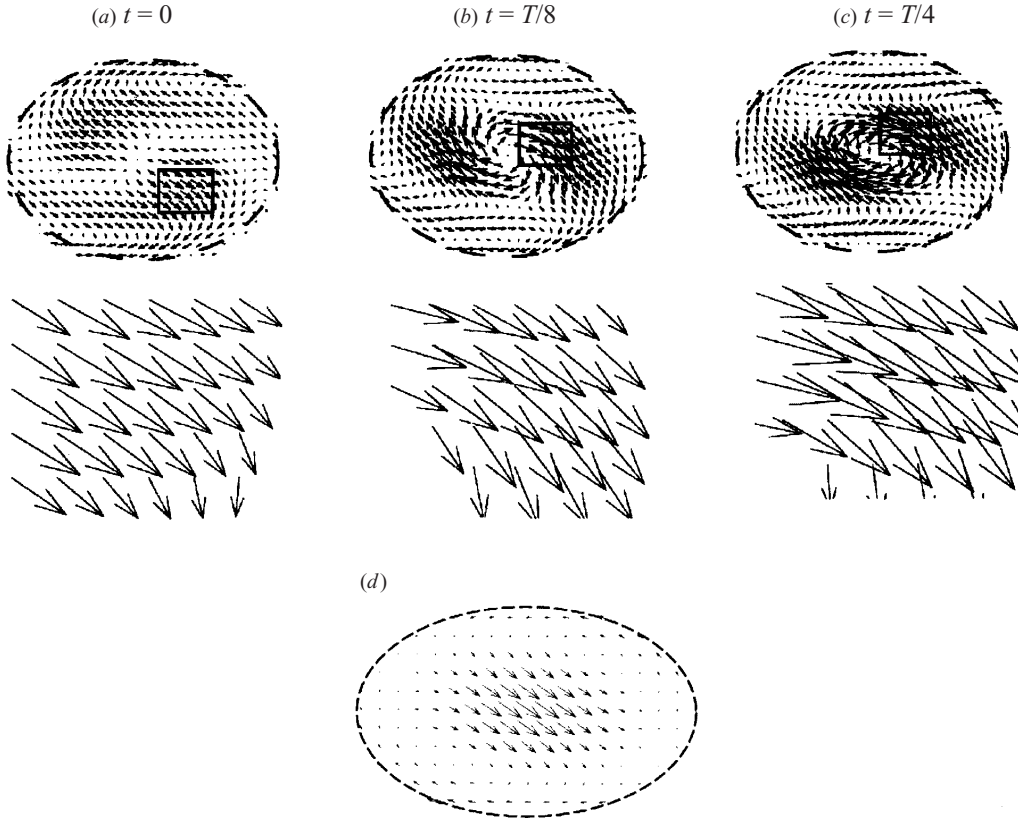


FIGURE 9. Eigenmode ω_{\perp} distribution in the $z_{\pi/2}$ -plane (see figure 1b). (a–c) CDI eigenmode of figure 8; (d) BW. (a) $t = 0$ (maximum area variation; no coiling of vortex lines), (b) $t = T/8$, (c) $t = T/4$ (no core area variation; maximally coiled vortex lines). Box in a–c encloses a patch of fluid with strain–vorticity locking. Expanded view of box is displayed underneath. Dashed lines are $\Omega_z = 0.2\Omega_0$ contour.

lines) and $t = T/4$ (no core area variation; maximally coiled vortex lines), where T is the oscillation period. When the core is most expanded, there is an elliptic region of $-\omega_z$ at the axis, surrounded by two regions of $+\omega_z$. When vortex lines are maximally coiled, there are four azimuthally distributed cells of alternately signed ω_z . The $\omega_{\perp} \equiv (\omega_r, \omega_{\theta})$ distribution is shown in figure 9 at three phases of the oscillation: $t = 0$, $T/8$, and $T/4$. At each stage, there are two patches of fluid with $\omega_{\perp} \equiv (\omega_r, \omega_{\theta})$ along the stretching direction of the external strain. One of the patches is marked by a box with its expanded view underneath. The patch moves in the $+\theta$ -direction, i.e. in the direction of the column's fluid angular velocity, from $\theta = 5\pi/4$ to $\theta = \pi/4$ during the time $t = 0$ to $t = T/4$. This is similar to the Rankine vortex eigenmode in figure 6. Sustained stretching due to strain–vorticity locking causes perturbation growth. The similarity between the Rankine and Gaussian-like vortex eigenmodes suggests that the instability is insensitive to the profile of vorticity or strain, and hence generic to vortices in external strain. Note however that unlike the Rankine vortex, the ω_{\perp} stretching rate is not uniform in the vortex core, as shown in figure 7(b). This non-uniformity causes the vorticity amplification rate to be different at the different phases of the oscillation in figure 9(a–c). The perturbation energy growth rate consequently oscillates, as discussed below.

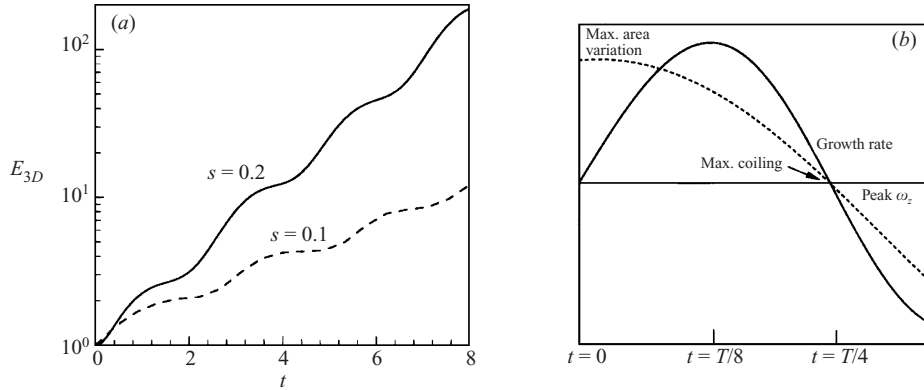


FIGURE 10. (a) CDI E_{3D} evolution for $k = 1$, $Re = 5000$.
 (b) Evolution of ω_z and E_{3D} growth rate in CDI.

CDI energy growth. The instantaneous growth rate of three-dimensional energy E_{3D} is not steady, but oscillates with twice the frequency of the CD oscillation and increases with increasing shear strength s (figure 10). To understand the oscillatory growth, we plot in figure 10(b) the instantaneous growth rate $d(\log E_{3D})/dt$, whose average over one period is $2\sigma_r$. The figure also shows the peak of perturbation vorticity ω_z (at the axis in the z_0 -plane; see figure 1b). When ω_z is large, so is the core area variation and when ω_z is zero on the axis, there is no core area variation. The growth rate is the largest at the phase ($t = T/8$) intermediate to those of maximum core variation and maximum vortex line coiling (figure 10). Insight into the growth rate oscillation is obtained by examining the ω_\perp stretching rate in regions of locking. Recall that the strain field is azimuthally non-uniform, with the maximum strain rate being on the major axis of the elliptic core and the minimum strain rate on the minor axis (figure 7b). Fluid with strain-vorticity locking lies in the region of the largest strain at $t = T/8$ (figure 9b). This is also the phase at which the growth rate is the largest. At other phases, the stretching is weaker, and hence the instantaneous growth rate.

Faster growth of BW. In this flow, BW growth rate is approximately twice that of CDI. To understand this, we consider the strain rate due to the external shear (estimated by taking the azimuthal average of the distribution in figure 7b). The interaction between the vortex (3.1) and the shear (3.2) makes the strain rate radially non-uniform. The strain rate is the largest on the vortex axis, where it is ≈ 3 times that outside the core and decreases with increasing radius. In BW, strain-vorticity locking occurs at the axis, as shown in figure 9(d). In CDI, on the other hand, locking occurs away from the axis (figure 9a-c) and therefore in regions of weaker strain than in BW. The weaker stretching of ω_\perp in CDI causes the instability to grow more slowly than in BW. This explanation is only qualitative; nevertheless, it is consistent with the nearly identical growths of BW and CDI in the Rankine vortex, where the strain rate is uniform in the core.

In the following, we describe the instability characteristics by varying in turn the three parameters: the perturbation axial wavenumber k , the relative shear strength s ($\equiv \gamma/\Omega_0$), and Re ($\equiv \Gamma/\nu$).

Variation of σ with k . Figure 11 shows the dependence on k of growth rate σ_r and oscillation frequency σ_i , with the relative shear strength s and Re held constant. There is an inviscid low- k cutoff, at $k \approx 0.5$. For $k > 2$ (figure 11a), the growth rate decreases due to viscous damping. There is a viscous high- k cutoff (not shown), which should

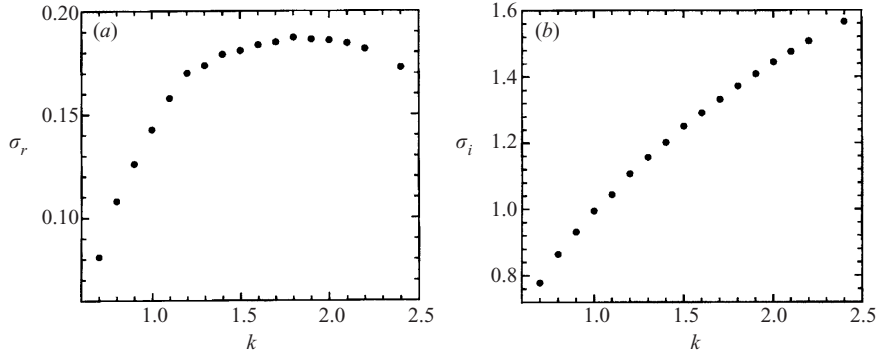


FIGURE 11. Dependence of CDI growth rate σ_r (a) and frequency σ_i (b) on axial wavenumber k . $s = 0.1$ and $Re = 5000$.

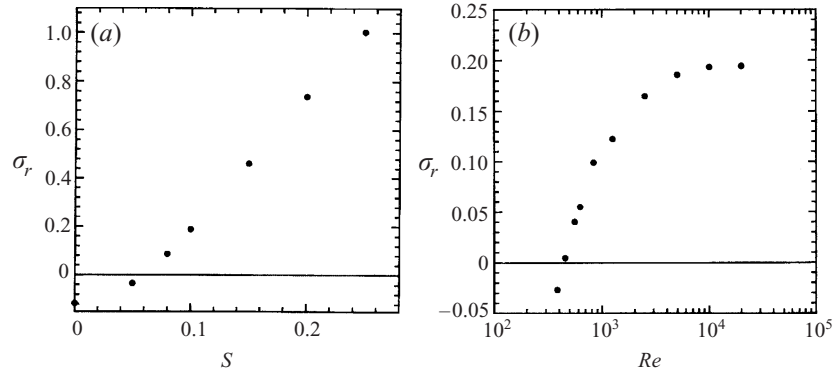


FIGURE 12. Dependence of CDI growth rate on: (a) relative shear strength s ($\equiv \gamma/\Omega_0$) for $Re = 5000$; and (b) Re for $s = 0.1$. Axial wavenumber $k = 2$.

increase with decreasing viscosity. There is a range of k values ($1.4 < k < 2.2$) in which the growth rate is nearly independent of k . This range should increase with decreasing viscosity. This ‘broadband’ growth behaviour is significant because a wide range of lengthscales can amplify equally. Therefore, a turbulent flow can result via nonlinear instability of an elliptic eddy.

Figure 11(b) shows that σ_i increases with increasing k . This increase is consistent with the strain–vorticity locking mechanism of growth. With increasing k , regions of large perturbation vorticity are increasingly confined closer to the vortex axis. Locking occurs progressively closer to the vortex axis, and hence in regions of increasing angular velocity. As the CD oscillation time period equals the time in which fluid with locking rotates once around the axis, σ_i increases with k . This argument suggests a finite upper limit for σ_i (equal to $\Omega_0/2$)—such a limit has been observed in the inviscid Stuart vortex (Schoppa *et al.* 1995).

Variation of σ with relative shear strength s and Re . Here we fix $k = 2$ and vary s and Re in turn. The dependence of σ_r on s and Re reflects the competition between viscous damping and inviscid amplification. First, consider the case when s is varied, by varying the shear strength γ while keeping Ω_0 is constant, and Re is held fixed (figure 12a). As expected, growth is progressively faster with increasing s . There is however no perturbation growth unless the shear strength is larger than a low- s cutoff value ($s \simeq 0.06$ in this case). The low- s cutoff value should decrease with

decreasing viscosity and the instability should occur for even infinitesimal external strain in the inviscid limit (as in the Rankine vortex). Note that the linear increase σ_r for $0.1 < s < 0.25$ suggests that higher-order terms of the weak-strain-asymptotic expansion of § 2 (i.e. $O(\epsilon^2)$ and higher) do not affect the growth rate.

Figure 12(b) shows the variation of σ_r with Re (here viscosity is changed while the shear strength is held fixed). There exists a low- Re cutoff ($\simeq 400$), below which viscous damping prevents perturbation growth. The growth rate becomes nearly independent of Re above a certain value, $Re \simeq 3000$; such behaviour is of course characteristic of inviscid instability.

4. Nonlinear CDI

4.1. Initial condition

An initially axisymmetric vortex column (3.1) is given a sinusoidal variation of core radius, with the vorticity distribution given by

$$\omega_z = G\left(\frac{r}{r_0\xi(z)}\right) \frac{r}{\xi(z)^3} \frac{d\xi}{dz}, \quad \omega_r = G\left(\frac{r}{r_0\xi(z)}\right) / \xi(z)^2, \quad \omega_\theta = 0, \quad (4.1)$$

where ω_z , ω_r and ω_θ are the total vorticity components (we hereinafter use lower-case symbols for all flow quantities), r_0 is the unperturbed vortex radius, and r the radial coordinate. The core vorticity profile $G(r)$ is compact Gaussian (3.1). The shape of the perturbed vortex core $\xi(z)$ is given by

$$\xi(z) = 1 - \mu \cos kz,$$

where μ is the perturbation amplitude and k the perturbation axial wavenumber. The peak unperturbed axial vorticity value $\Omega_0 = 1$. As in § 3, the vortex (4.1) is embedded in uniform shear flow: $u_x(y) = -\gamma y$. The base flow is shown schematically in figure 1(b). As the flow is non-axisymmetric, a Cartesian (x, y, z) coordinate system shown in figure 1(b) is also used.

Flow evolution is obtained via direct numerical simulation (DNS). The parameter values used were: relative shear strength $s \equiv \gamma/\Omega_0 = 0.1$, $k = 1$, $\mu = 0.1$, and vortex Reynolds number $Re = 5000$. DNS (with 128^3 grid points) is performed using a Fourier pseudospectral algorithm, with periodic boundary conditions in x and z , and semi-periodic boundary conditions in y (see Appendix C for DNS details). The initial vortex diameter is one-third of the domain size (spanning 42 grid points).

Because the perturbation is sinusoidal, the flow has certain symmetries. There are z -planes in which $\omega_r = \omega_\theta = \partial\omega_z/\partial z \equiv 0$, which are a half the perturbation wavelength $\lambda/2$ apart, e.g. planes z_0 and z_π in figure 1(b). These planes are material, i.e. u_z is always identically zero on these, and core size variation is maximum in these planes, and the cores expand and contract periodically in an out-of-phase manner. In the following, we visualize the flow in these two symmetry planes to understand CDI evolution. We also visualize the meridional y -plane passing through the vortex axis, in which ω_y is parallel/anti-parallel to ω_θ .

4.2. Large-amplitude CDI oscillation

While the nature of the CDI oscillation remains unchanged at large amplitudes, there are significant nonlinear effects. To illustrate this, we plot ω_z contours in z_0 and z_π (figure 13) over a period of one CDI oscillation and the corresponding meridional flow (in terms of ω_θ) in figure 14. Note that panels (b–f) in figure 13 correspond respectively to panels (b–f) in figure 14.

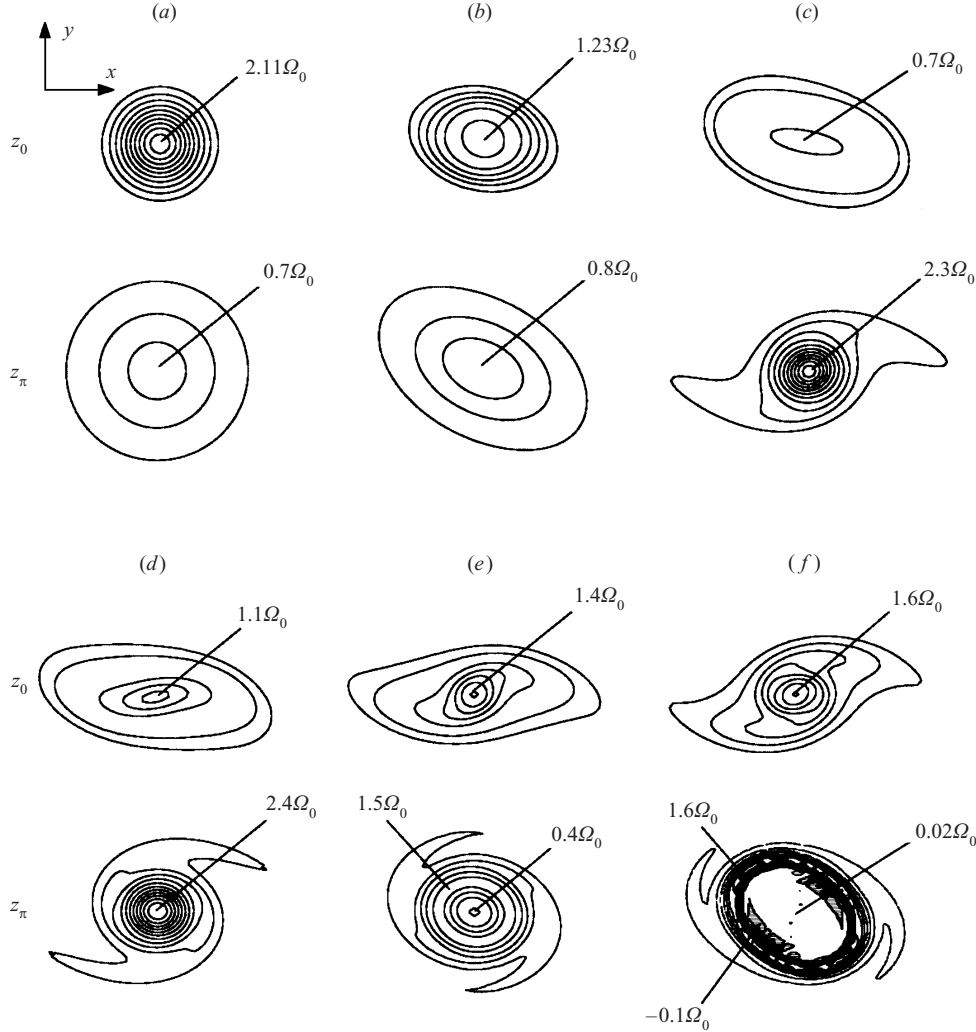


FIGURE 13. Evolution of ω_z in z_0 - and z_π -planes (see figure 1b) during one CDI oscillation. (a) $t = 0$, (b) 1, (c) 2, (d) 3.5, (e) 5, (f) 6.

Initially, the core size in z_0 is much smaller than in z_π (figure 13a). Immediately thereafter (figure 13b), two effects become evident. First, shear distorts the axisymmetric vortex core into an elliptic one. Secondly, vorticity magnitude ω is reduced in z_0 and increased in z_π (figure 13b). The differential swirl between z_0 and z_π generates azimuthal vorticity ω_θ , whose distribution (figure 14b) is such that fluid is pumped away from z_π in both directions, resulting in vortex stretching at z_π and compression at z_0 (recall the z -periodicity of the flow). As vortex stretching/compression continues, the differential swirl between z_0 and z_π decreases, and momentarily becomes zero. However, as $|\omega_\theta|$ has continually increased until this instant, the axial flow continues to stretch/compress ω_z in the two cores. (This stage of the oscillation is analogous to figure 4c.) Thus, peak ω_z in z_π becomes larger than in z_0 (figure 13c). The differential swirl, now reversed, first reduces the magnitude of ω_θ and then changes its sign. In linear CDI, ω_θ reversal occurs simultaneously everywhere along the column. In non-linear CDI, however, the reversal is non-uniform, with reversed (say, secondary) ω_θ

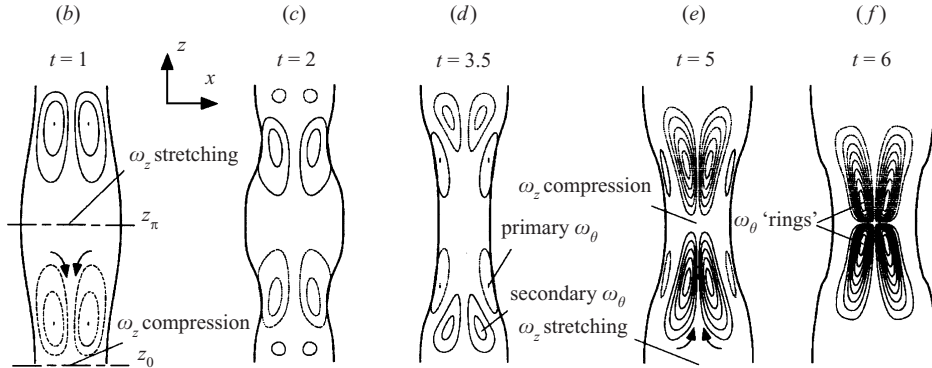


FIGURE 14. ω_θ contours in the meridional y -plane (see figure 1b) illustrating the oscillation of ω_θ in response to the ω_z variation shown in figure 13. Panels (b–f) correspond respectively to panels (b–f) in figure 13. Outer contour is vorticity magnitude $\omega = 0.2\Omega_0$.

first appearing near z_0 (figure 14c, d). (As we shall see later, z -dependent ω_θ reversal is crucial to the eventual transition.) Secondary ω_θ stretches ω_z in z_0 , while the lingering unreversed (say, primary) ω_θ continues to stretch ω_z in z_π , evident from ω values in figure 13(c, d). The regions of secondary ω_θ increase in size, and the secondary ω_θ magnitude also increases (figure 14d, e). Primary ω_θ magnitude is simultaneously reduced, and it eventually disappears (figure 14f).

Note that we have interpreted ω_θ reduction in figure 14 only in terms of the differential swirl, i.e. in terms of an inviscid mechanism. Viscous diffusion also contributes to ω_θ reduction, especially in regions with large vorticity gradients. For example, there is annihilation of primary ω_θ and secondary ω_θ between z_0 and z_π (figure 14d, e). More importantly, viscous annihilation of the two colliding ‘rings’ across the z_π plane (figure 14f) further reduces secondary ω_θ . At large Re , ω_θ reduction via annihilation is however expected to be much smaller than that via the reversal of the differential swirl.

Self-advection of ω_θ . In nonlinear CDI, the self-advection of ω_θ , i.e. by self-induced velocity u_z , becomes prominent—like the self-induced motion of a vortex ring. Two such secondary ω_θ ‘rings’ (coaxial with the column) appear, one on either side of z_π (figure 14d), and both rings move toward z_π (figure 14e, f).

During this process of self-advection, differential swirl continues to increase secondary $|\omega_\theta|$. Simultaneously, there is additional increase of $|\omega_\theta|$ via mutually induced stretching of the two colliding rings (quite similar to the ‘head-on collision’ of coaxial axisymmetric vortex rings; see Stanaway, Shariff & Hussain 1988). This process is shown schematically in figure 15(a, b). The two oppositely signed ω_θ rings (figure 15a) move toward z_π by self-advection and are simultaneously stretched as they collide (figure 15b), with their radii increasing, and their cores becoming more circular (and smaller).

The evolution of the ω_θ rings subsequent to figure 14(f) is shown in figure 16. The ring core develops a head–tail shape, with weaker vorticity being left behind due to the more rapid self-advection of the stronger vorticity in the head (figure 16a, b). The concomitant increase of ring radius (illustrated in figure 15b, c) is evident in figure 16(a, b). The increase of $|\omega_\theta|$ is opposed by the uncoiling of vortex lines following the reversal of the differential swirl and also by cross-diffusion across z_π . These effects become progressively stronger as ω_θ becomes increasingly localized near

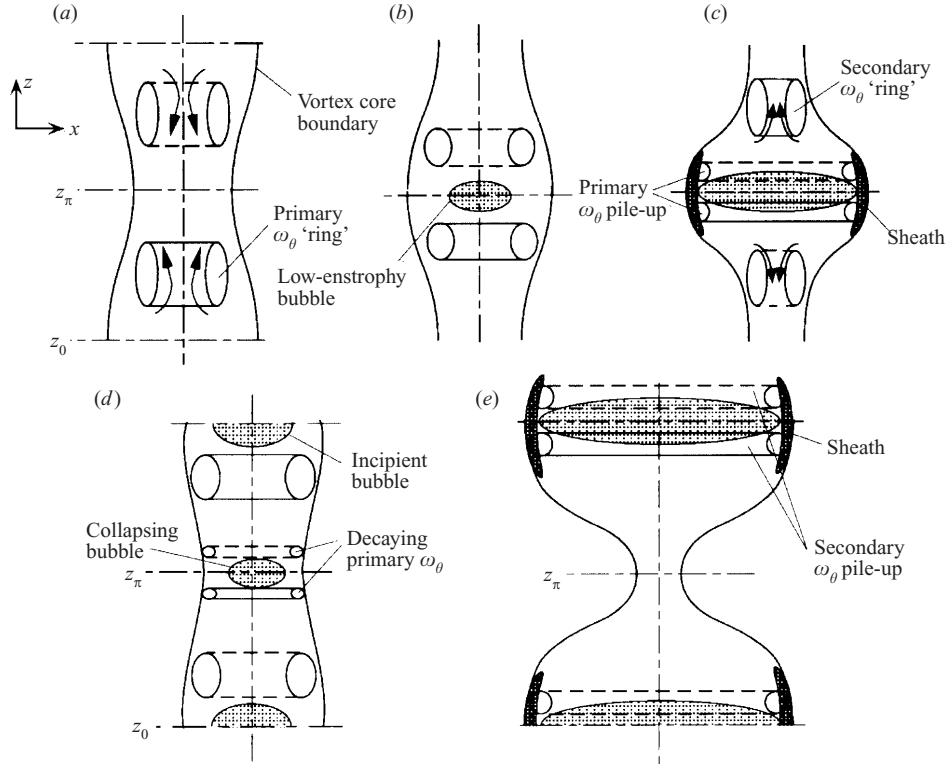


FIGURE 15. Illustration of primary ω_θ and secondary ω_θ self-advection leading to successive sheath formation and collapse alternately, in each plane z_0 and z_π (see figure 1b).

z_π (figure 16a–c) and soon overcome the stretching-induced ω_θ intensification. As a result, ω_θ magnitude now begins to decrease (figure 16c).

Thus, self-advection and mutual stretching of the rings lead to a ‘pile-up’ (i.e. localization and intensification) of ω_θ near z_π (figures 15c, 16c). The effect of pile-up on ω_z is discussed below.

4.3. Sheath dynamics

Sheath formation. As ω_θ piles up, there is intense compression of ω_z near z_π (figure 13d–f). The magnitude of ω_z on the column axis decreases rapidly, rendering the core nearly irrotational. Ring-induced $+u_r$ advects ω_z radially outward. The meridional flow being circulatory, there is a radius outside which u_z is oppositely directed and stretches ω_z there (figure 15c). Thus, peak ω_z location in z_π is shifted away from the axis (figure 13e). Core vorticity thus becomes organized into a thin annular sheath surrounding a nearly irrotational region. Vorticity compression in the core is so intense that ω in the bubble is nearly a 100 times smaller than in the sheath (figure 13f). Concomitant with sheath formation, there is also opposite-to-mean (negative) ω_z generation in the low-entropy bubble (figure 13f). This is discussed later in § 4.4.

While the pile-up occurs, ω_θ stretches the core in z_0 (figure 13d–f). Progressive stretching in z_0 once again reverses the differential swirl. The subsequent meridional flow reversal leads to sheath ‘collapse’, as discussed below.

Sheath collapse. To illustrate sheath collapse, figure 17 shows ω_z contours and velocity (u_x, u_y) vectors in plane z_π at times immediately subsequent to those in

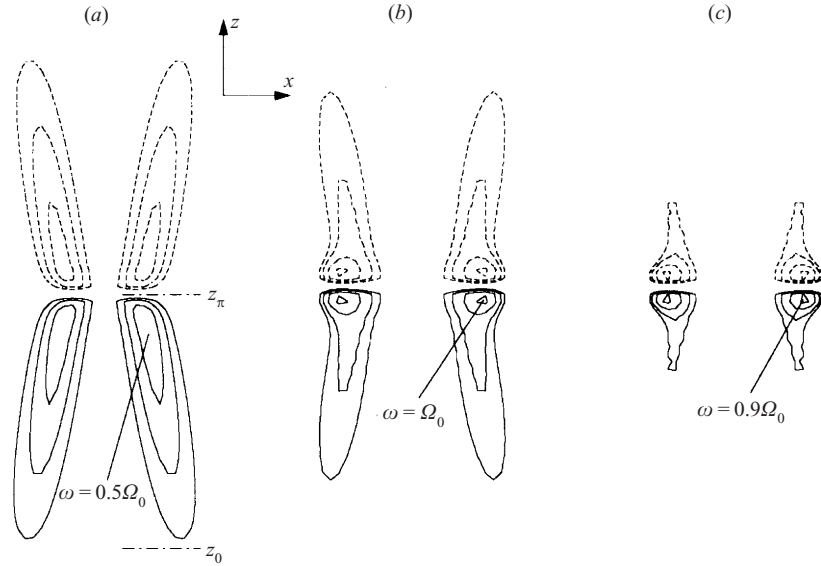


FIGURE 16. The evolution of ω_θ in the meridional y -plane showing the effect of mutually induced stretching of the ω_θ 'rings'. This sequence immediately follows figure 14(f). (a) $t = 6.25$, (b) 6.50, (c) 6.80.

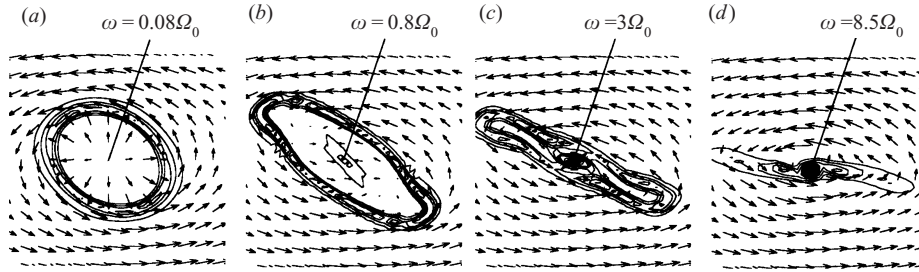


FIGURE 17. ω_z contours and velocity (u_x, u_y) vectors in the z_π -plane (see figure 1b) illustrating sheath collapse.

figure 13. Figure 17(a) shows a time prior to the meridional flow reversal. Shortly thereafter, reversed ω_θ near the sheath induces meridional flow in the opposite direction than before, and u_r in z_π begins to be directed radially inward (figure 18b). As secondary ω_θ intensifies (figure 18c), the intensifying reversed meridional flow causes strong stretching of residual (weak) vorticity in the bubble. Thus, ω_z magnitude at the bubble axis increases rapidly, and soon it exceeds sheath ω_z , forming a new core vortex (figure 17c). Azimuthal velocity u_θ induced by ω_z near the axis begins to distort the sheath shape, and sheath vorticity is wrapped around the core vortex. Eventually, the core once again becomes compact, with the vorticity peak on the axis (figure 17d).

Meanwhile, secondary ω_θ is also generated away from the sheath (between z_0 and z_π in figure 18c). Self-advection of this secondary ω_θ subsequently causes pile-up near z_0 (figure 18d), leading to the development of a sheath near z_0 . As CDI amplifies, sheaths form and collapse periodically in z_0 and z_π (in an out-of-phase manner) with every meridional flow reversal. Self-advection of secondary ω_θ , after a sheath is formed (say, in plane z_π), becomes prominent at earlier phases of successive oscillations. That is,

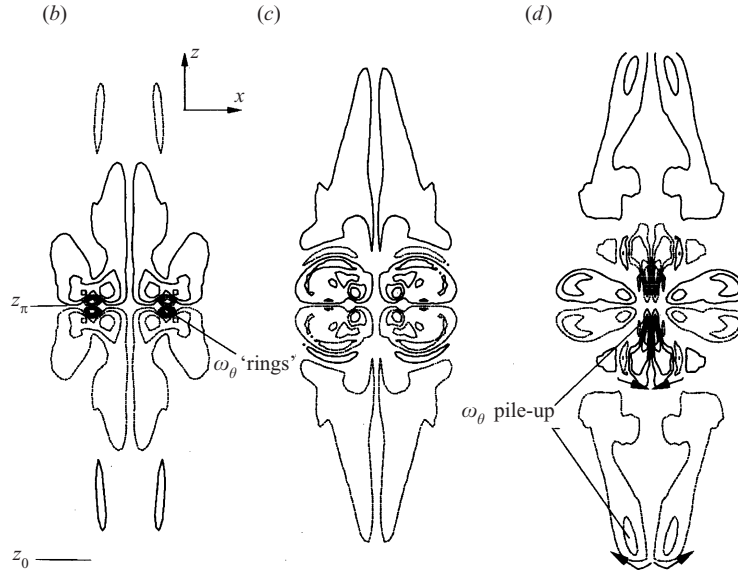


FIGURE 18. Evolution of ω_θ contours in the meridional y -plane (see figure 1b) illustrating the self-advection of secondary ω_θ away from the sheath in z_π (figure 17). Panels (b–d) correspond respectively to panels (b–d) in figure 17.

secondary ω_θ advects away from a sheath even as sheath collapse occurs. This process is shown schematically in figure 15(d). The subsequent pile-up of secondary ω_θ , via its self-advection, then forms a sheath near z_0 (figure 15e). The reversed meridional flow in the collapsing sheath (near z_π in figure 15d) progressively weakens in successive oscillations. Hence sheath collapse is rendered progressively slower. Also, as primary ω_θ self-advection is also progressively more rapid, sheaths form more quickly. Thus, in successive CDI periods, sheaths persist increasingly longer.

Sheath instability. As a result of increasing sheath longevity, there is more time for a Kelvin–Helmholtz-type instability to grow on the sheath. Incipient sheath instability is seen in figure 19(a, b) as wavy corrugations. These corrugations grow (figure 19c), culminating in the roll-up of the sheath into azimuthally distributed fine-scale ‘vortexlets’ (figure 19d). Vortex lines in the sheath, hence also the vortexlets, have a hairpin-like geometry (not shown) because of significant ω_θ in addition to ω_z .

Upon meridional flow reversal, $-u_r$ advects the vortexlets toward the column axis (figure 19d). Note that, unlike before (figure 17), ω_z in the core remains weak (figure 19e, f) as the self-advection of secondary ω_θ away from the sheath region has weakened vortex stretching in the core. Adjacent vortexlets coalesce in a succession of pairing events, and eventually all the vortexlets collapse into a single compact vortex core (figure 19g–i). As the vortexlets pair, their ω_θ magnitude is progressively reduced. Thus, the coalescing vortexlets are nearly rectilinear.

Summarizing, core areas half a perturbation wavelength $\lambda/2$ apart contract and expand periodically. The sequence of sheath formation, roll-up and pairing repeats. Thus, CD evolution involves both cascading (sheath formation and roll-up into vortexlets) and anti-cascading (pairing of vortexlets) events. Vortexlet length, measured along the axis, increases with each oscillation, for the following two reasons. First, the sheath extent along the column axis increases, because differential swirl generates increasingly intense meridional flow. Secondly, vortex lines in the sheath become

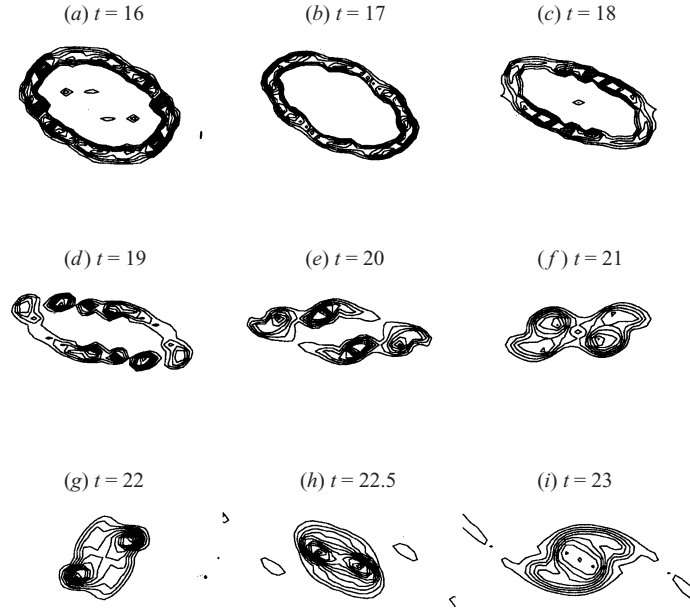


FIGURE 19. Evolution of ω_z contours in the z_0 plane (see figure 1b) showing sheath instability leading to roll-up into vortexlets (a–d), and sheath collapse via successive pairing of vortexlets into a single core (e–i).

increasingly curved, because of progressively amplifying ω_θ . The radius of the low-entropy bubble (in the region of core expansion) also increases in successive cycles.

4.4. Vortex line folding and reconnection

Opposite-to-mean (negative) ω_z generation (see, e.g., $-\omega_z$ in z_π in figure 13f) is an important aspect of transition because, while initially ω_z is positive everywhere, a turbulent flow contains vorticity of both signs in ω_z . Negative ω_z is due to the intense meridional flow in the low-entropy bubble; the streamline geometry is shown schematically in figure 20(a). In an inviscid flow, such a meridional flow will advect an inner-core vortex line towards the core periphery. The vortex line is stretched in the sheath and pressed together in the bubble, developing S-shaped kinks (figure 20a–c). As the folded vortex filament is pressed together, it will reconnect (in a viscous flow) and form a closed filament loop, thereby generating $-\omega_z$ in the z_π -plane (figure 20c). Note that because $u_z = \omega_x = \omega_y = 0$ in z_0 and z_π , $-\omega_z$ can be produced in these planes only by a viscous mechanism, i.e. reconnection.

This mechanism explains the opposite-to-mean vorticity (hence looping) in figure 21. Such vortex line geometry implies fine-scale granularity in the ω distribution that is a characteristic feature of developed turbulence. Although $-\omega_z$ first appears near sheaths, such vorticity develops all along the column axis, with progressively increasing CDI amplitude (hence increasingly intense ω_θ that can fold vortex filaments). Once opposite-to-mean vorticity has been generated, $-\omega_z$ is stretched by CDI-induced u_z , resulting in the progressive growth of the peak $-\omega_z$ in the flow (figure 22a).

4.5. Onset of transition

Vortex transition results via the two nonlinear-instability mechanisms discussed above: sheath formation and its roll-up into vortexlets, and vortex line folding and reconnection. Meridional flow intensity amplifies with each successive oscillation, as evidenced

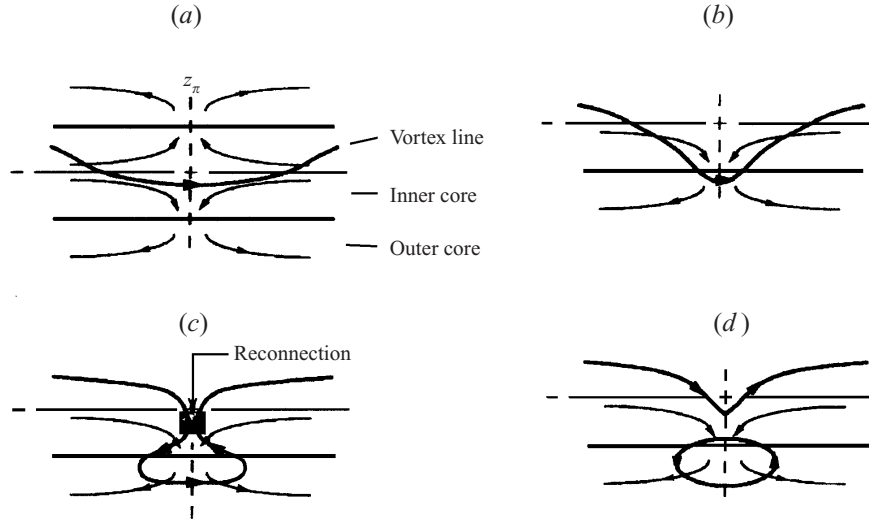


FIGURE 20. Schematic of vortex filament folding and subsequent reconnection, producing opposite-to-mean ω_z (from Schoppa *et al.* 1995).

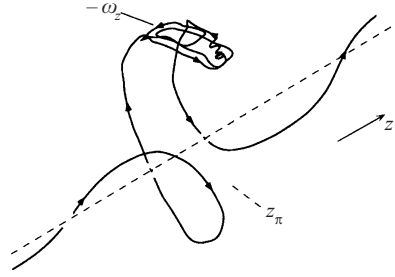


FIGURE 21. A vortex line through a region of $-\omega_z$ at $t = 23$.

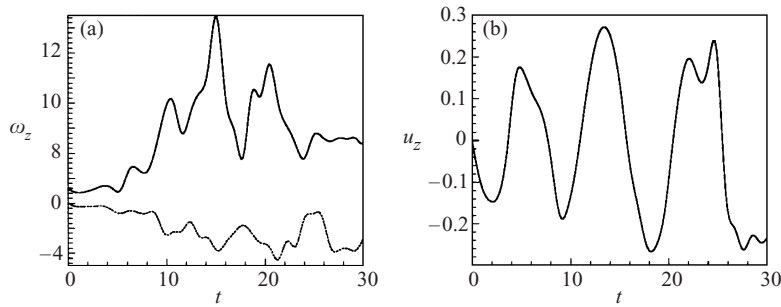


FIGURE 22. Evolution of pointwise velocity/vorticity: (a) positive (solid lines) and negative (dotted lines) ω_z domain peak; (b) $u_z(0,0,z_{\pi/2})$.

by the evolution of u_z intensity on the column axis in the $z_{\pi/2}$ -plane (figure 22b). In linear CDI, this is the location of the domain peak of u_z at all phases of the oscillation. In nonlinear CDI, ω_θ pile-up leads to the shifting of peak u_z location toward z_0 or z_π , and peak u_z at times $t > 16$ is even larger than in figure 22(b). After $t \simeq 20$, peak u_z in the flow even exceeds peak u_θ (i.e. vortex swirl).

Recall that with amplifying CDI, the intensifying self-advection of ω_θ causes pro-

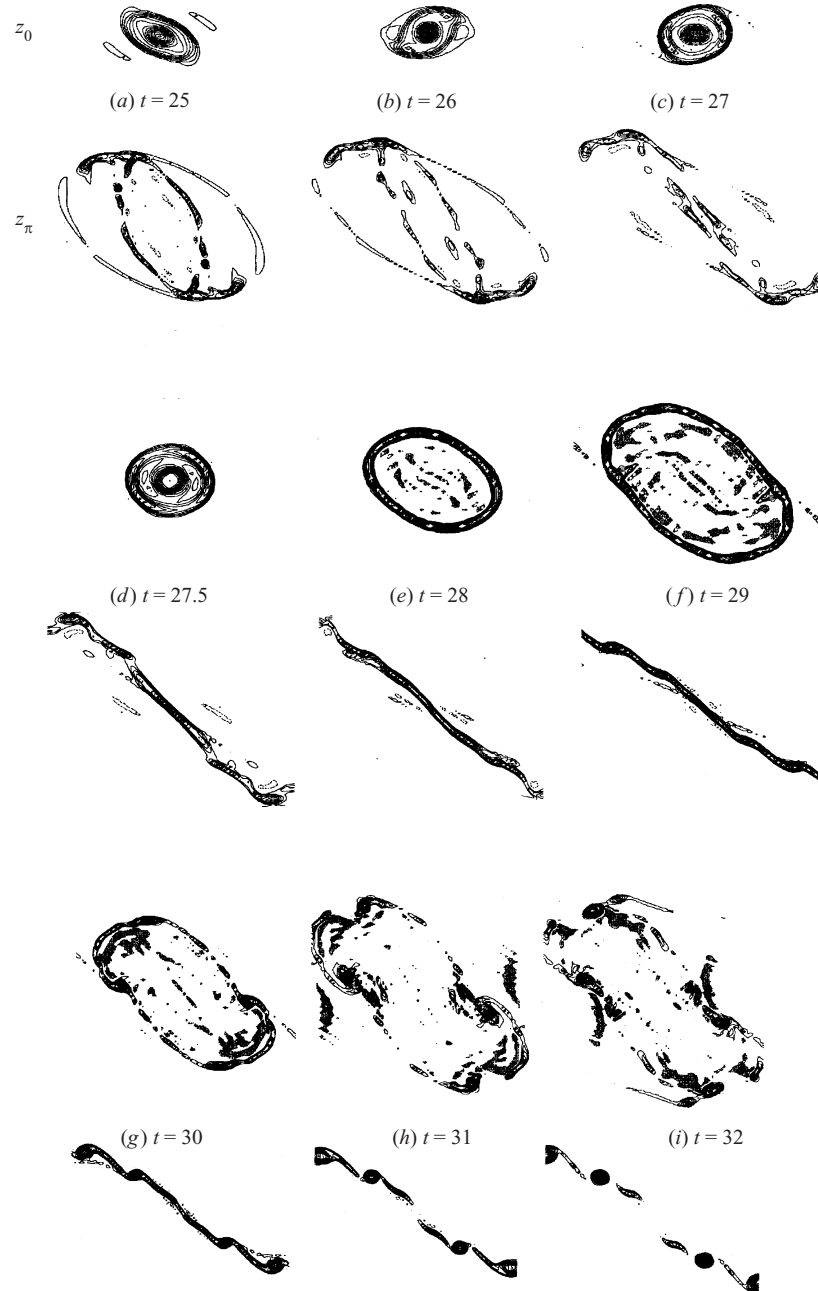


FIGURE 23. ω_z contours illustrating the onset of transition via the roll-up of vortex sheaths in both the symmetry planes: z_0 (top) and z_π (bottom) (see figure 1b). Shaded regions contain $-\omega_z$.

gressively faster sheath formation and progressively slower sheath collapse. Secondary ω_θ advection eventually becomes so rapid that even while the sheath is rolling up at one z -plane, collapse has not happened $\lambda/2$ away. This process leads to nearly simultaneous roll-up all along the column.

In figure 23(a), we can see a compact vortex core in z_0 and a sheath in z_π . The cumulative effect of advection by the background shear and the radially inward

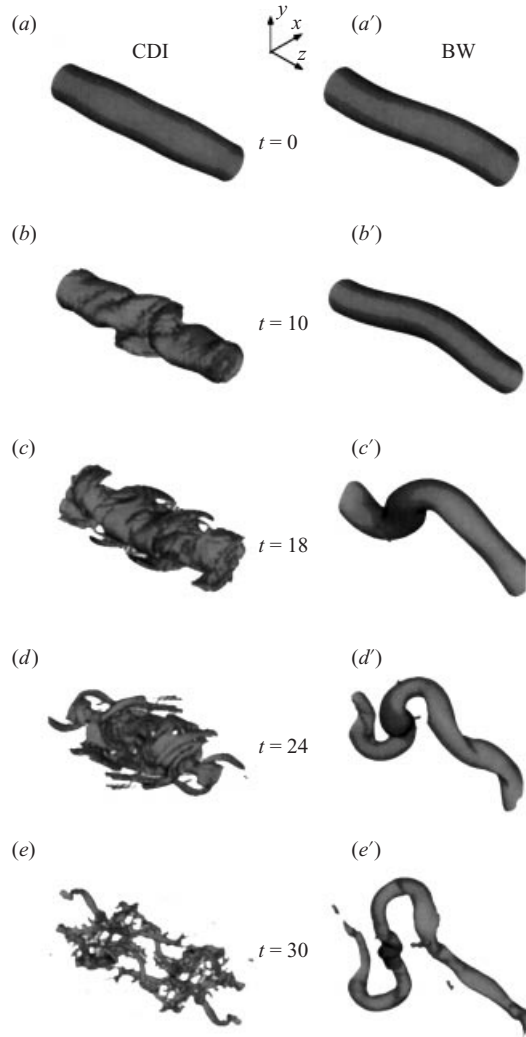


FIGURE 24. Isovorticity surfaces for CD ($a-e$) and BW ($a'-e'$) instabilities with time increasing downwards. Surfaces are plotted at: $|\omega| = 0.5\Omega_0$ ($a-c$, $a'-c'$); $|\omega| = 0.8\Omega_0$ (d,d'); and $|\omega| = 1.4\Omega_0$ (e,e').

meridional flow in z_π causes the sheath vorticity to become organized into a sheet-like structure (figure 23*a-f*). Simultaneously, the meridional flow compresses core vorticity in z_0 , forming a vortex sheath. Both these structures, i.e. the sheath in z_0 and the vortex sheet in z_π , then undergo roll-up into finer-scale vortices (figure 23*g-i*). The simultaneous roll-up in both symmetry planes means that the vortex core is now nowhere compact. The coupling between the differential swirl and the meridional flow is weakened, and the sheaths' collapse is preempted by the disruption of the vortex column's CD.

In figure 24($a-e$), we summarize CDI evolution in terms of isovorticity surfaces. (Figure 24($a'-e'$) shows BW evolution that is discussed in § 5.) Figure 24(e) shows that the vortexlets formed by sheath roll-up are elongated tubular vortices. Figure 25(a) shows a rake of five vortex lines started within one of these structures. The fine-scale

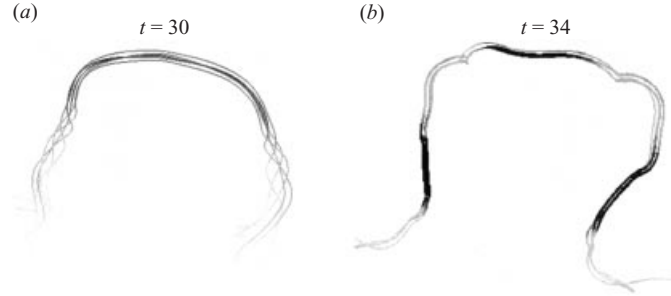


FIGURE 25. Vortex lines, grey-scaled on vorticity magnitude, plotted through one of the fine-scale filaments of figure 23(f).

vortex then develops core area variation, i.e. CD, of its own (figure 25b), as indicated by high (dark) and low (light) vorticity along the bundle. The vortex also develops twists (clear in visualization), suggesting that a BW is also triggered. It is likely that these perturbations, induced by the adjacent vortex filaments, will amplify if their vortex Re is sufficiently large to overcome viscous damping. In this manner, a self-similar CDI (or BW) instability can generate progressively finer scales in a cascade scenario.

5. Comparison of BW and CDI evolutions

So far, we have focused on CDI, i.e. on explaining the effect of axial inhomogeneity of a vortex column's core size or vorticity. If both CDI and BW are triggered, one would expect that BW, owing to its faster growth, causes a more rapid transition than CDI. This is not necessarily the case, as discussed below.

We study BW instability on the same base flow (3.1), (3.2) as CDI. The vortex axis is given a sinusoidal deflection (of axial wavenumber $k = 1$) of amplitude $0.1r_0$ in the plane of stretching, where r_0 is the unperturbed core radius. For comparison between BW and CDI, all flow parameters are kept the same, i.e. the relative shear strength $s(\equiv \gamma/\Omega_0) = 0.1$ and the Reynolds number $Re(\equiv \Gamma/\nu) = 5000$.

Nonlinear BW evolution. Figure 24(a'–e') depicts BW evolution via isovorticity surfaces. For comparison, the left-hand column shows CDI evolution at corresponding times. (Different vorticity levels are chosen at different times for better clarity; the same level is used for both BW and CDI at each time.) The vortex axis, deflected by the perturbation, lies in the plane of stretching (figure 24a'), i.e. the plane formed by the stretching direction of the external strain and the unperturbed column axis. Perturbation vorticity aligned with the strain is continually stretched, hence the growth of BW (figure 24b', c'). Until $t \simeq 24$, the vortex remains in the plane. Afterwards, vortex segments near the wave crests develop larger curvature than elsewhere (figure 24d'). The enhanced self-induced velocity of these segments (with elliptic cross-sections) tilts them out of the plane of stretching; this is evident by $t = 24$ (figure 24d'). This out-of-plane tilting is the primary nonlinear instability effect until this time. The BW continues to grow in amplitude and the vortex core near the wave crests becomes increasingly elliptic, i.e. increasingly sheet-like. Upon further evolution, these sheets should eventually develop a Kelvin–Helmholtz-type instability (see Lundgren & Mansour 1996; Rogers & Moser 1992). The computation was performed up to $t = 36$; beyond this time, the vortex interference effects (namely, the image effect of

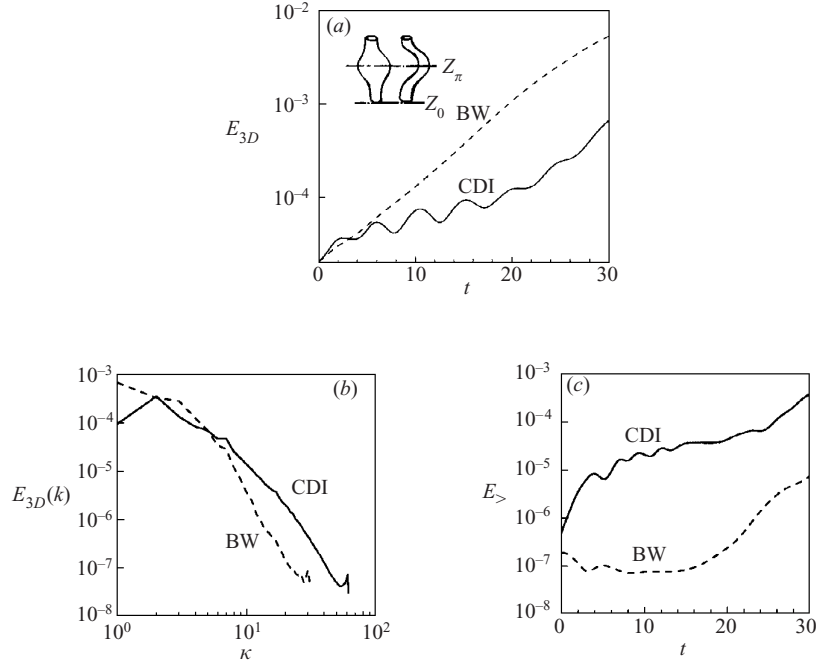


FIGURE 26. Comparison of CDI (solid) and BW (dashed) energetics: (a) total three-dimensional energy $E_{3D}(t)$ (inset shows symmetry z -planes); (b) spectra of E_{3D} at $t = 30$, where $\kappa \equiv (k_x^2 + k_y^2 + k^2)^{1/2}$; and (c) fine-scale energy $E_{>}$.

the impenetrable boundary condition and interaction between vortices from adjacent boxes), not a goal of our study, will become significant.

The contrast between BW and CDI in promoting transition is vivid at $t = 30$ (figure 24e,e'). The vortex column breaks down into numerous fine-scale vortices in CDI. On the other hand, BW deforms the vortex continually, and the column persists as a single (elongated) large-scale structure. To analyse the difference between the two instabilities, we now consider three-dimensional energy.

Three-dimensional energy. As expected from linear instability features, BW shows faster growth of three-dimensional perturbation energy E_{3D} (figure 26a). (E_{3D} is the total three-dimensional energy, consisting of all wavenumbers (except $k = 0$) in all directions.) By $t = 30$, BW contains nearly 10 times as much energy as CDI. Note that modes with $k > 1$ (finer scales) are also excited in the nonlinear stage. In BW, energy in the fundamental mode ($k = 1$) is about 60% of E_{3D} by $t = 30$ (with the remainder contained in modes with $k > 1$). In CDI, energy in the fundamental mode is only about 20% of E_{3D} . That is, there is faster fine-scale growth in CDI. The primary mechanism for this is the self-advection of $\omega_{\hat{\theta}}$ (discussed in §4.2), causing pile-up near planes z_0 and z_π (see figures 1b, 26a). For example, while the $\omega_{\hat{\theta}}$ distribution in figure 14(e) has most of the energy in $k = 1$ mode, the subsequently piled-up $\omega_{\hat{\theta}}$ (figure 16c) is mostly in $k > 1$ modes.

Note that CDI's E_{3D} oscillates in time at a frequency twice that of BW. That is, there are times of decreasing E_{3D} when there is also enhanced energy dissipation. The mechanism of the temporary E_{3D} decay as well as the damping of the E_{3D} oscillation with increasing time requires further investigation. The BW being non-oscillatory, there is a monotonic growth of E_{3D} .

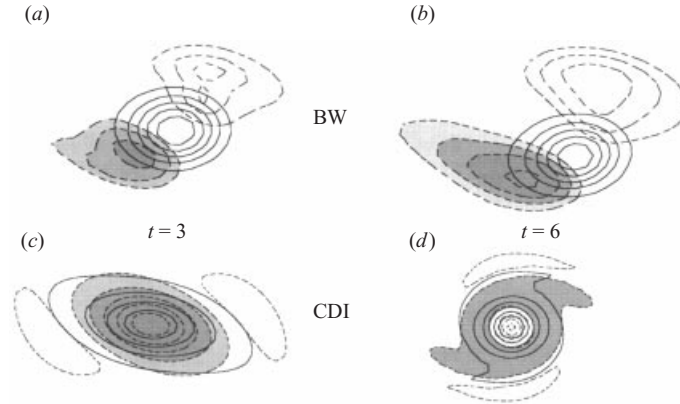


FIGURE 27. Contours of vorticity (solid lines) and $\partial u_z/\partial z$ (dashed lines) in z_0 (see figure 1b). BW instability: (a) $t = 3$, (b) $t = 6$; CDI: (c) $t = 3$, (d) $t = 6$. Shaded regions have $+\partial u_z/\partial z$.

Fine-scale energy. Despite the lower level of three-dimensional energy in CDI, figure 24 suggests that fine-scale energy is larger in CDI than in BW. This is confirmed by comparing the spectra of E_{3D} (figure 26b) at a late stage of the evolution ($t = 30$). We see that although the BW contains more E_{3D} at small wavenumbers $\kappa < 10$ (where $\kappa \equiv (k_x^2 + k_y^2 + k^2)^{1/2}$ is the wavenumber magnitude of an (x, y, z) Fourier mode), CDI has more energy in the higher- κ range. The evolution of fine-scale energy $E_>$ (denoting three-dimensional energy in modes with $\kappa > 10$) is shown in figure 26(c). While there is virtually no growth of BW's $E_>$ up to $t = 12$, there is rapid growth right from the beginning in CDI.

This difference in the fine-scale growth is explored by comparing vortex stretching in the two instabilities. In CDI, regions of the largest strain rate and largest vorticity magnitude coincide; in BW, however, these regions are spatially separated. (Such coincidence in CDI causes more intense enstrophy production, and hence more rapid fine-scale growth). In the nonlinear stage of the instability, self-stretching exceeds the external strain and hence is the dominant mechanism of fine-scale growth.

To capture the essence of the self-stretching effect, we focus on a symmetry z -plane (say, z_0 or z_π in figure 1b), where vortex stretching (entirely due to self-stretching, i.e. $\omega_z \partial u_z / \partial z$) is the largest. Note that the external strain makes no contribution to enstrophy production in these planes.

First, consider BW. Figure 27(a), where vorticity and $\partial u_z / \partial z$ contours are plotted, shows that regions of large strain rate are away from the vortex column axis, i.e. occurring in regions of weak vorticity. Further, as a fluid particle moves around the axis, vorticity is alternately stretched and compressed. Therefore, total enstrophy production in the core via self-stretching is nearly zero, and the peak vorticity magnitude remains nearly the same after a period of 3τ (where τ is the eddy turnover time) (figure 27b).

Now consider CDI. Self-stretching is centred on the column axis (figure 27c), i.e. in regions of large vorticity magnitude. Such stretching at the axis makes the expanded core shown in figure 27(c) into a compact structure (figure 27d), which becomes progressively more compact in successive cycles. The vorticity magnitude in the core is increased and the vortex core size is reduced. This implies that there is greater fine-scale energy in the core than before. Thus, self-stretching in CDI, in contrast to BW, produces finer-scaled, intense core vorticity (see figure 17d, for example).

In addition to the coincidence of large strain and vorticity, the peak strain rates are

also larger (by a factor of $\simeq 5$) in CDI. This also contributes to CDI's faster fine-scale generation. The self-stretching will increase with increasing k in both instabilities. Will CDI self-stretching continue to be higher than in BW? This needs further study. However, we expect the answer to be positive, as the nonlinear effects observed here should remain qualitatively the same.

The comparison between BW and CDI shows that faster instability growth need not imply faster transition. Even when BW and CDI are triggered at comparable amplitudes, transition could occur via CDI.

6. Concluding remarks

An axisymmetric perturbation to a vortex column evolves as an oscillation of the column's core size or vorticity (i.e. core dynamics, CD). The axial variation of azimuthal velocity, inherent to core size perturbation, causes vortex lines to coil and hence induce meridional flow, having both radial and axial velocity components. Coupling between meridional flow and the vortex's differential swirl leads to repetitive coiling and uncoiling of vortex lines (§ 2.2 and figure 4). Without any external strain, CD is neutrally stable in an inviscid flow and decays in a viscous flow. With an external equatorial strain, the CD oscillation can amplify exponentially. This CD instability (CDI) is possible because the column's axial vorticity is tilted to generate radial and azimuthal components (ω_r , ω_θ), which can then be stretched by the strain.

The physical mechanism of instability is clarified by the analysis of a weakly strained Rankine vortex. The axisymmetric perturbation – the azimuthal wavenumber $m = 0$ wave – and the strain interact to generate $m = \pm 2$ waves. Instability occurs when $m = 0$ and $m = 2$ (or $m = 0$ and $m = -2$) waves resonate. There are numerous (discrete) resonant frequencies, and the growth rate varies with the frequency value. Strongest growth results when the CD oscillation frequency equals the vortex's fluid angular velocity. At this frequency, strain–vorticity locking occurs, i.e. the perturbation vorticity of a fluid particle remains aligned with the stretching direction *at all times*. Because the perturbation is azimuthally and axially sinusoidal, locking occurs on a double helix. That is, at any instant in time, the helix at one z -plane has only ω_r , but has only ω_θ in a z -plane a quarter perturbation wavelength $\lambda/4$ away, and so on.

Strain–vorticity locking is not restricted to CD (i.e. $m = 0$ perturbation) alone, but occurs for all m (including $m = \pm 1$, i.e. BW). Hence a large variety of unstable modes is possible, the instability oscillation frequency depending on m . The growth of perturbations with $|m| > 1$ can result in unusual vortex behaviour, e.g. ‘braiding’ – the breakup of a vortex into a number of helical strands – which has been observed in turbulence (Cadot *et al.* 1995).

CD growth via strain–vorticity locking also occurs in a Gaussian-like vortex, verifying that the instability mechanism, insensitive to the profile of strain or vorticity, is generic. Instability growth rate is proportional to the strain rate, which decreases with increasing radius. As locking occurs on the vortex axis in BW, but away from the axis in CDI, BW grows faster than CDI. The perturbation-damping effect of viscosity causes low- s (strain rate), low- Re (Reynolds number) and high- k (axial wavenumber) instability cutoffs. The competition between inviscid amplification and viscous damping implies that (a) the high- k cutoff value should increase with increasing Re or increasing s ; (b) the low- Re cutoff value should decrease with increasing s ; and (c) the low- s cutoff value should decrease with increasing Re .

In nonlinear CDI, the self-advection (via u_z) and stretching (via u_r) of azimuthal vorticity ω_θ generate intense axial strain in the core. Consequently, the compact vor-

tex core is organized into a thin annular sheath surrounding a low-*enstrophy* bubble (figure 13*f*). The sheath undergoes a Kelvin–Helmholtz-type roll-up into azimuthally distributed fine-scale ‘vortexlets’. Upon meridional flow reversal, the vortexlets are advected radially inward and coalesce in a succession of pairing events; all the vortexlets eventually ‘collapse’ into a single compact vortex core. The sequence of sheath formation, roll-up and collapse repeats, as the vortex column core areas $\lambda/2$ apart contract and expand periodically, in an out-of-phase fashion. Thus, nonlinear CDI involves simultaneous cascading (sheath formation and roll-up) and anti-cascading events (vortexlet pairing). With amplifying CDI, progressively stronger self-advection of ω_θ causes both faster sheath formation and slower subsequent sheath collapse (due to the weakening meridional flow, §4.3). Eventually, self-advection becomes so rapid that even while a sheath is rolling-up, collapse has not occurred $\lambda/2$ away. The vortex core is now nowhere compact, and the coupling between meridional flow and differential swirl is reduced, preventing the collapse of vortexlets (§4.5). Because of the disrupted CDI, the flow contains numerous elongated vortexlets (of length $\approx \lambda$). Vortex lines plotted through vortexlets show significant variation of vorticity magnitude. That is, vortexlets have in turn their own CD and would undergo transition via self-similar CDI, if their Reynolds number were sufficiently high. This self-similar transition scenario presents itself as a candidate for a physical-space cascade process in developed turbulence. Additional random fine-scale vorticity is generated via the folding and subsequent reconnection of core vortex filaments, resulting in opposite-to-mean axial vorticity $-\omega_z$. Thus, a turbulent flow results with ‘worm’-like vortices (vortexlets) as well as fine-scale vorticity granularity.

In vortices with nearly homogeneous (cylindrical) cores, one would expect that the faster-growing BW instability would lead to a more rapid transition than CDI. Analysis of nonlinear BW evolution, however, indicates quite the contrary. We have tried to understand this enigmatic result in terms of vortex stretching in the two flows. The growth of fine-scale energy occurs via self-stretching. In BW, self-stretching occurs in the core periphery, where the vorticity magnitude is low. On the other hand, CDI-induced self-stretching occurs near the axis, where vorticity magnitude is large. This difference seems to account for the faster fine-scale growth in CD. Thus, in a flow where CD and BW are triggered at comparable amplitudes and even when BW has larger initial growth rate, CD-induced mechanisms would seem to dominate fine-scale growth and transition. This conjecture deserves further investigation.

Nonlinear CDI in stretched vortices is of interest because of their prevalence in turbulence. Axial stretching inhibits instability by decreasing the perturbation axial wavenumber k , eventually causing the perturbation to leave the unstable band (Eloy & Le Dizès 1999). The rapid growth of high- k waves in CDI, however, makes it likely that they will remain in the unstable band and hence that transition in stretched vortices results via CDI.

Our results appear relevant to the dynamics of the intense fine-scale vortices (worms) that occur in turbulence. Worms have segments with compression as well as segments with stretching. A vortex subjected to such straining develops CD; the compressed segments are organized into sheaths, and roll-up of sheaths will occur in worms of sufficiently high vortex Re (which scales as $Re_\lambda^{1/2}$). The mechanism of worm formation is enigmatic (see, e.g., Jiménez & Wray 1998) because worm azimuthal velocity $u_\theta \simeq u'$ (r.m.s. velocity of total turbulence), implying that worms cannot be formed from a larger vortex (having $u_\theta = u'$) by direct stretching (which increases u_θ). The vortexlets from sheath roll-up have $u_\theta \approx u'$ (of the parent vortex), suggesting CDI as the primary mechanism of worm formation.

CDI is relevant to fully developed turbulence phenomena in other contexts as well. First, consider vortex reconnection. Segments of reconnected vortices (bridges) show strong core inhomogeneity, which can grow via the strain induced by the conjugate bridge or the segments of unreconnected vortices (threads) (Melander & Hussain 1988; Virk, Hussain & Kerr 1995). The CD-induced (meridional) flow will influence bridge and thread motion, on which the completeness of reconnection and the reconnection timescale depend sensitively. Because reconnection, in turn, triggers CD, the two cascade mechanisms—reconnection and CDI—are thus coupled. It therefore appears necessary to incorporate CD in the analysis of reconnection, which we presume is prevalent in developed turbulence. Second, CDI is likely to be triggered on a coherent structure (CS) via the structure's interaction with ambient fine-scale turbulence. The fine scales are organized into an array of ring-like threads (Melander & Hussain 1993a), which can excite CD on the structure (Marshall 1997). The growth of CD (possible via either an orthogonal strain as studied here or resonance of CD with ring motion (Miyazaki & Hunt 2000)) may explain why coherent structures are often strongly polarized. Analysis using helical wave decomposition—which separates the right- and left-handed components of a vector field—should yield significant insight into (i) how regions of strong polarization can develop in an initially unpolarized flow, and (ii) interactions between polarized large and fine scales (this interaction is presumably dependent on the extent of polarization of both (Melander & Hussain 1993b)).

Finally, the turbulent flow resulting from CD-transition can serve as a tractable case in which to analyse the dynamical features of transitional flows and fully developed turbulence. The relative simplicity of this flow (containing well-defined structures) should not only facilitate the study of physical-space structures but also help address issues such as: the dependence of strain–vorticity alignment on the strain–vorticity ratio, the role of vortex-like and sheet-like structures in cascade and dissipation, and the dynamics of worms.

Financial support from NSF through grants CTS-9622302 and CTS-9904328 is gratefully acknowledged. Supercomputer time was provided by NASA Ames Research Center. F.H. acknowledges support during the 1999 Turbulence Program at the Isaac Newton Institute, Cambridge, UK and the 2000 Hydrodynamic Turbulence Program at the Institute for Theoretical Physics, UCSB. We thank Prashant Haldipur for careful review of the manuscript.

Appendix A. Solution of the $O(\epsilon^1)$ problem for Rankine vortex CD

We describe here the $O(\epsilon^1)$ solution. By inserting the $O(\epsilon^0)$ solution in the governing equations, and by eliminating the velocity components, we obtain the equation satisfied by the $O(\epsilon^1)$ pressure perturbation within the core:

$$r^2 \frac{dp_m^{(1)}}{dr^2} + r \frac{dp_m^{(1)}}{dr} + (\eta_m^2 r^2 - m^2) p_m^{(1)} = C_m, \quad m = 0, 2. \quad (\text{A } 1)$$

The forcing terms C_m , given in terms of the $O(\epsilon^0)$ solution, appear on the right-hand side. They are

$$C_0 = -\frac{8\sigma^{(1)}}{\sigma^{(0)3}} k^2 r^2 J_0(\eta_0 r) \alpha_0 + \left[\frac{\sigma^{(0)} + 4i}{(\sigma^{(0)} + 2i)^2} i k^2 r^2 J_0(\eta_2 r) + 4 \frac{\sigma^{(0)} + i}{\sigma^{(0)2} (\sigma^{(0)} + 2i)^2} i k^2 \eta_2 r^3 J_1(\eta_2 r) \right] \alpha_2, \quad (\text{A } 2a)$$

$$C_2 = \left[-\frac{\sigma^{(0)} - 2i}{\sigma^{(0)2}} ik^2 r^2 J_2(\eta_0 r) + 4 \frac{\sigma^{(0)} + i}{\sigma^{(0)2}(\sigma^{(0)} + 2i)^2} ik^2 \eta_0 r^3 J_1(\eta_0 r) \right] \alpha_0 - \frac{8\sigma^{(1)}}{(\sigma^{(0)} + 2i)^3} k^2 r^2 J_2(\eta_2 r) \alpha_2. \quad (\text{A } 2b)$$

Note that since C_m are evaluated at the crossing-points, the subscript m has been dropped from $\sigma^{(0)}$.

Closed form solutions (non-singular at $r = 0$) to the pressure equation can be written in the form

$$p_0^{(1)} = J_0(\eta_0 r) \gamma_0 + \sigma_0^{(1)} B_0 \alpha_0 + \bar{B}_0 \alpha_2, \quad p_2^{(1)} = J_2(\eta_2 r) \gamma_2 + \sigma_2^{(1)} B_2 \alpha_2 + \bar{B}_2 \alpha_0, \quad (\text{A } 3)$$

where γ_m ($O(\epsilon^1)$ mode amplitude) is the constant of integration. The coefficients B_m represent the effect of strain in modifying the oscillation frequency of mode m , whereas \bar{B}_m represent the effect on one m -mode of the interaction between the strain and the other m -mode.

Terms B_m and \bar{B}_m in (A 3) are as follows:

$$B_0 = -\frac{4k^2 r}{\sigma^{(0)3} \eta_0} J_1(\eta_0 r), \quad (\text{A } 4a)$$

$$\begin{aligned} \bar{B}_0 = & \frac{i\pi k^2 (\sigma^{(0)} + 4i)}{2(\sigma^{(0)} + 2i)^2} [Y_0(\eta_0 r) \int^r t J_0(\eta_2 t) J_0(\eta_0 t) dt - J_0(\eta_0 r) \int^r t J_0(\eta_2 t) Y_0(\eta_0 t) dt] \\ & + \frac{2\pi i (\sigma^{(0)} + i) k^2 \eta_2}{\sigma^{(0)2} (\sigma^{(0)} + 2i)^2} [Y_0(\eta_0 r) \int^r t^2 J_1(\eta_2 t) J_0(\eta_0 t) dt - J_0(\eta_0 r) \int^r t^2 J_1(\eta_2 t) Y_0(\eta_0 t) dt], \end{aligned} \quad (\text{A } 4b)$$

$$B_2 = -\frac{4k^2 \sigma^{(1)}}{(\sigma^{(0)} + 2i)^3} \left(\frac{2J_2(\eta_2 r)}{\eta_2^2} - \frac{r J_1(\eta_2)}{\eta_2} \right), \quad (\text{A } 4c)$$

$$\begin{aligned} \bar{B}_2 = & -\frac{i\pi k^2 (\sigma^{(0)} - 2i)}{2\sigma^{(0)2}} [Y_2(\eta_2 r) \int^r t J_2(\eta_0 t) J_2(\eta_2 t) dt - J_2(\eta_2 r) \int^r t J_2(\eta_0 t) Y_2(\eta_2 t) dt] \\ & + \frac{2\pi i k^2 (\sigma^{(0)} + i) \eta_0}{\sigma^{(0)2} (\sigma^{(0)} + 2i)^2} [Y_2(\eta_2 r) \int^r t^2 J_1(\eta_0 t) J_2(\eta_2 t) dt - J_2(\eta_2 r) \int^r t^2 J_1(\eta_0 t) Y_2(\eta_2 t) dt]. \end{aligned} \quad (\text{A } 4d)$$

Here, Y_0 and Y_2 are Bessel functions of the second kind of order 0 and 2.

The potential flow outside the core satisfies

$$\frac{d^2 \phi_m^{(1)}}{dr^2} + \frac{1}{r} \frac{d\phi_m^{(1)}}{dr} - \frac{m^2}{r^2} \phi_m^{(1)} - k^{(0)2} \phi_m^{(1)} = 0, \quad m = 0, 2,$$

whose solution $\phi_m^{(1)}$ (non-singular at ∞) is

$$\phi_m^{(1)} = K_m(k^{(0)} r) \delta_m, \quad m = 0, 2, \quad (\text{A } 5)$$

where δ_m are constants of integration. Note that we have dropped the subscript m on k since we only consider the crossing-points.

Enforcing the boundary conditions to match the inner and outer solutions, we

obtain the relationship between the integration constants γ_m and δ_m ,

$$\begin{pmatrix} k^{(0)}K'_m & -\mathcal{A}_m \\ (\sigma_m^{(0)} + im)K_m & J_m \end{pmatrix} \begin{pmatrix} \delta_m \\ \gamma_m \end{pmatrix} = \begin{pmatrix} G_m \\ H_m \end{pmatrix}, \quad m = 0, 2. \quad (\text{A } 6)$$

The terms G_m and H_m are given in terms of the $O(\epsilon^0)$ solution.

The matrix has non-trivial solutions to the homogeneous problem (neutrally stable waves). Therefore, solutions to (A 6) must satisfy a solvability condition, which is the expression for the growth rate, $\sigma^{(1)}$.

Appendix B. Strain–vorticity locking in Rankine vortex eigenmodes

We present an argument here that there are oscillation frequencies for any resonant combination of m and $m + 2$ (Kelvin) waves that satisfy the sufficient condition for strain–vorticity locking:

$$\frac{D\boldsymbol{\omega}_\perp}{Dt} = 0, \quad (\text{B } 1)$$

where $\boldsymbol{\omega}_\perp \equiv (\omega_r, \omega_\theta)$ and $D/Dt \equiv (\partial/\partial t + \mathbf{U} \cdot \nabla)$, with $\mathbf{U} = (0, U_\theta, 0)$ being the vortex velocity field.

When the strain and the perturbation both have vanishingly small magnitudes, advection is due to U_θ alone (advection of $\boldsymbol{\omega}_\perp$ by \mathbf{u} and the straining flow being negligible). That is, a fluid particle traces a circular path around the vortex axis with a (scaled) angular velocity of 1. Hence, only the azimuthal coordinate θ_L (subscript L indicating a Lagrangian variable) of a fluid particle varies with time, and $\theta_L = t + \psi$, where ψ is the initial azimuthal location. For such a fluid particle, $D\hat{r}/Dt = \hat{\theta}$ and $D\hat{\theta}/Dt = -\hat{r}$. For such a fluid particle (B 1) implies that

$$d\omega_{rL}/dt = \omega_{\theta L}, \quad d\omega_{\theta L}/dt = -\omega_{rL},$$

where ω_{rL} and $\omega_{\theta L}$ are material vorticity components. These equations have the solution

$$\omega_{rL} = A \cos(-t), \quad \omega_{\theta L} = A \sin(-t). \quad (\text{B } 2)$$

We now show that resonant combinations can be formed which satisfy this strain–vorticity locking condition.

At these crossing-points where $\sigma^{(0)} = -i(m + 1)$ (and also, $\eta_m^2 = \eta_{m+2}^2 \equiv \eta^2$), the m -wave has perturbation vorticity distribution

$$\left. \begin{aligned} \omega_{r,m}^{(0)} &= i \left(\frac{2km}{r} J_m(\eta r) - \frac{2}{3} k \eta J_{m-1}(\eta r) \right) \alpha_m \\ \omega_{\theta,m}^{(0)} &= \left(\frac{2km}{r} J_m(\eta r) - \frac{4}{3} k \eta J_{m-1}(\eta r) \right) \alpha_m \end{aligned} \right\}, \quad (\text{B } 3)$$

and the $(m + 2)$ -wave has perturbation vorticity distribution

$$\left. \begin{aligned} \omega_{r,m+2}^{(0)} &= -i \left(\frac{2k(m+2)}{3r} J_{m+2}(\eta r) + \frac{2}{3} k \eta J_{m+1}(\eta r) \right) \alpha_{m+2} \\ \omega_{\theta,m+2}^{(0)} &= \left(-\frac{2k(m+2)}{3r} J_{m+2}(\eta r) + \frac{4}{3} k \eta J_{m+1}(\eta r) \right) \alpha_{m+2} \end{aligned} \right\}. \quad (\text{B } 4)$$

Taking $\alpha_m = -i$ (without loss of generality) and $\alpha_{m+2} = ie^{i\delta}$ (the phase difference

between the two waves), we obtain the vorticity fields

$$\left. \begin{aligned} \omega_r &= \left[\frac{2km}{r} J_m - \frac{2k\eta}{3} J_{m-1} \right] \cos(kz + m\theta - (m+1)t) \\ &\quad + \left[\frac{2k(m+2)}{3r} J_{m+2} + \frac{2k\eta}{3} J_{m+1} \right] \cos(kz + (m+2)\theta - (m+1)t + \delta), \\ \omega_\theta &= \left[\frac{2km}{r} J_m - \frac{4k\eta}{3} J_{m-1} \right] \sin(kz + m\theta - (m+1)t) \\ &\quad + \left[\frac{2k(m+2)}{3r} J_{m+2} - \frac{4k\eta}{3} J_{m+1} \right] \sin(kz + (m+2)\theta - (m+1)t + \delta). \end{aligned} \right\} \quad (\text{B } 5)$$

Now, we replace θ by $\theta_L = t + \psi$ to obtain the vorticity components of a fluid particle that initially is at $\theta = \psi$. For particles on a helix given $\psi = -kz/(m+1)$, (B 5) reduce to

$$\omega_{r,L} = \frac{2k}{3} [(m+2)J_{m+2} - mJ_m] \cos\left(\frac{kz}{m+1} - t\right), \quad (\text{B } 6a)$$

$$\omega_{\theta,L} = \frac{2k}{3} [(m+2)J_{m+2} - mJ_m] \sin\left(\frac{kz}{m+1} - t\right). \quad (\text{B } 6b)$$

This vorticity distribution satisfies the strain–vorticity locking condition (B 2). It is easily verified that ω_\perp has the same orientation everywhere on the helix. If this orientation is along the strain’s stretching direction, perturbation growth will occur.

This heuristic argument shows that resonant combinations of modes m and $m+2$ will be unstable at least for those values of k at which their oscillation frequencies equal $(m+1)$. Thus the instability mechanism operates for all m and, in particular, for CDI ($m=0$).

Appendix C. DNS algorithm

The DNS code integrates the Navier–Stokes equations using a Fourier–pseudospectral algorithm which requires periodic boundary conditions in x and z . In the transverse direction y , a free-slip, impermeable boundary condition is imposed, which is implemented using half-range sine expansions for u_x and u_z , and a cosine expansion for u_y . Time-stepping is performed using the leap-frog scheme with an occasional Euler step to dampen its weak numerical instability. The computational domain is a cube of dimension $(2\pi)^3$. The initial vortex core diameter ($2r_0$) is restricted to approximately one-third of the box dimension to minimize the effect of vortices in neighbouring boxes while maintaining adequate spatial resolution.

Since the shear profile (3.2) has a discontinuous gradient at $y = 0$ and 2π , the profile is slightly modified to be of the form,

$$\Omega_{shear} = \frac{\gamma}{2} \left[1 + \tanh\left(\frac{\pi - \delta_1 - |y - \pi|}{\delta_2}\right) \right],$$

which is a top-hat profile for vorticity; δ_1 governs the location where vorticity takes half its peak value, and δ_2 the rate at which it decays to zero at the top and bottom walls. Their values are chosen such that shear vorticity is nearly uniform in the vicinity of the vortex core.

For linear stability analysis, the code is modified to solve the linearized equation

$$\frac{\partial \mathbf{u}}{\partial t} = -\mathbf{U} \cdot \nabla \mathbf{u} - \mathbf{u} \cdot \nabla \mathbf{U} - \frac{1}{\rho} \nabla p + \nu \nabla^2 \mathbf{u}, \quad (\text{C } 1a)$$

$$\nabla \cdot \mathbf{u} = 0, \quad (\text{C } 1b)$$

where lower-case quantities are the perturbation, which is of the form

$$\mathbf{u} = \tilde{\mathbf{u}}(x, y, t) e^{ikz}. \quad (\text{C } 2)$$

The axial wavenumber k is held fixed in any given run. The simulation is initialized with a divergence-free white-noise (in the z -plane) perturbation $\tilde{\mathbf{u}}$ and integrated in time by solving

$$\frac{\partial \hat{\mathbf{u}}}{\partial t} = \mathbf{P}(\mathbf{k}) \cdot (\tilde{\mathbf{u}} \times \hat{\boldsymbol{\Omega}} + \mathbf{u} \times \hat{\boldsymbol{\omega}}) - \frac{\mathbf{k} \cdot \mathbf{k}}{\nu} \hat{\mathbf{u}}, \quad (\text{C } 3)$$

where $\hat{}$ represents the Fourier transform of a variable and $\mathbf{P}(\mathbf{k}) \equiv (\mathbf{I} - \mathbf{k}\mathbf{k}/|\mathbf{k}|^2)$ is the projection tensor that ensures divergence-free velocity. The linear stability code is easily obtained from the nonlinear solver by converting three-dimensional FFTs to two-dimensional FFTs, by freezing the base flow and by modifying the routines where the right-hand side of (C 3) is computed (Billant *et al.* 1999).

The perturbed base flow is then integrated in time. Upon integrating for a fairly long period ($\approx 200\tau$), the most unstable eigenmodes become energetically dominant. The flow is integrated until the growth rate of three-dimensional energy,

$$\sigma_r \equiv 0.5 \, d \ln E_{3D} / dt$$

becomes steady. While only the most unstable mode (in our case, the BW) is directly accessible using this technique, the CDI eigenmode can be obtained via orthogonalization (Mamun & Tuckerman 1995). The validity of the CDI eigenmode is checked by perturbing the base flow with this mode alone and checking the steadiness of both the growth rate and the oscillation frequency.

REFERENCES

- ARENDT, S., FRITTS, D. & ANDREASSEN, O. 1997 The initial value problem for Kelvin vortex waves. *J. Fluid Mech.* **344**, 181.
- BATCHELOR, G. K. 1967 *An Introduction to Fluid Dynamics*. Cambridge University Press.
- BAYLY, B. J. 1986 Three-dimensional instability of an elliptical flow. *Phys. Rev. Lett.* **57**, 2160.
- BILLANT, P., BRANCHER, P. & CHOMAZ, J.-M. 1999 Three-dimensional stability of a vortex pair. *Phys. Fluids* **11**, 2069.
- CADOT, O., DOUADY, S. & COUDER, Y. 1995 Characterization of low pressure filaments in a three-dimensional turbulent shear flow. *Phys. Fluids* **7**, 630.
- ELOY, C. & LE DIZÈS, S. 1999 Three-dimensional instability of Burgers and Lamb-Oseen vortices in a strain field. *J. Fluid Mech.* **378**, 145.
- ELOY, C., LE GAL, P. & LE DIZÈS, S. 2000 Experimental study of the multipolar vortex instability. *Phys. Rev. Lett.* **85**, 3400.
- GLEDZER, E. B. & PONOMEREV, V. M. 1992 Instability of bounded flows with elliptical streamlines. *J. Fluid Mech.* **240**, 1.
- HUSSAIN, F. 1998 Core dynamics instability of a vortex in shear: a physical-space cascade mechanism. *Bull. Am. Phys. Soc.* **43**, 2004.
- JIMÉNEZ, J., MOFFATT, H. K. & VASCO, C. 1996 The structure of vortices in freely decaying two dimensional turbulence. *J. Fluid Mech.* **313**, 209.
- JIMÉNEZ, J. & WRAY, A. A. 1998 On the characteristics of vortex filaments in isotropic turbulence. *J. Fluid Mech.* **373**, 255.

- JIMÉNEZ, J., WRAY, A. A., SAFFMAN, P. G. & ROGALLO, R. S. 1993 The structure of intense vorticity in isotropic turbulence. *J. Fluid Mech.* **255**, 65.
- KELVIN, LORD 1880 Vibrations of a vortex column. *Phil. Mag.* **10**, 155.
- KIDA, S. 1981 Motion of an elliptic vortex in a uniform shear flow. *J. Phys. Soc. Japan* **50**, 3517.
- LEBLANC, S. & CAMBON, C. 1998 Effects of the Coriolis force on the stability of Stuart vortices. *J. Fluid Mech.* **356**, 353.
- LEIBOVICH, S. & KRIBUS, A. 1990 Large amplitude wavetrains and solitary waves in vortices. *J. Fluid Mech.* **216**, 459.
- LEONARD, A. 1994 Nonlocal theory of area-varying waves on axisymmetric vortex tubes. *Phys. Fluids* **6**, 765.
- LEWEKE, T. & WILLIAMSON, C. H. K. 1998 Cooperative elliptic instability of a vortex pair. *J. Fluid Mech.* **360**, 85.
- LUNDGREN, T. S. & ASHURST, W. T. 1989 Area-varying waves on a curved vortex tube with application to vortex breakdown. *J. Fluid Mech.* **200**, 283.
- LUNDGREN, T. S. & MANSOUR, N. N. 1996 Transition to turbulence in an elliptic vortex. *J. Fluid Mech.* **307**, 43.
- MALKUS, W. V. R. 1989 An experimental study of the global instabilities due to the tidal (elliptical) distortion of a rotating elastic cylinder. *Geophys. Astrophys. Fluid Dyn.* **48**, 123.
- MAMUN, C. K. & TUCKERMAN, L. S. 1995 Asymmetry and Hopf bifurcation in spherical Couette flow. *Phys. Fluids* **7**, 80.
- MARSHALL, J. S. 1997 The flow induced by periodic vortex rings wrapped around a columnar vortex core. *J. Fluid Mech.* **345**, 1.
- MASON, D. M. & KERSWELL, R. R. 1999 Nonlinear evolution of the elliptical instability: an example of inertial wave breakdown. *J. Fluid Mech.* **396**, 73.
- MELANDER, M. V. & HUSSAIN, F. 1988 Cut-and-connect of two antiparallel vortex tubes. *CTR Rep.* S-21, p. 257.
- MELANDER, M. V. & HUSSAIN, F. 1993a Coupling between a coherent structure and fine-scale turbulence. *Phys. Rev. E* **48**, 2669.
- MELANDER, M. V. & HUSSAIN, F. 1993b Polarized vorticity dynamics on a vortex column. *Phys. Fluids A* **5**, 1992.
- MELANDER, M. V. & HUSSAIN, F. 1994 Core dynamics on a vortex column. *Fluid Dyn. Res.* **13**, 1 (referred to herein as MH).
- MIYAZAKI, T. & HUNT, J. C. R. 2000 Linear and nonlinear interactions between a columnar vortex and external turbulence. *J. Fluid Mech.* **402**, 349.
- MOFFATT, H. K., KIDA, S. & OHKITANI, K. 1994 Stretched vortices—the sinews of turbulence; large-Reynolds-number asymptotics. *J. Fluid Mech.* **259**, 241.
- MOORE, D. W. & SAFFMAN, P. G. 1975 The instability of a straight vortex filament in a strain field. *Proc. R. Soc. Lond. A* **346**, 413.
- PIERREHUMBERT, R. T. 1986 Universal short-wave instability of two dimensional eddies in an inviscid fluid. *Phys. Rev. Lett.* **57**, 2157.
- PIERREHUMBERT, R. T. & WIDNALL, S. E. 1982 The two- and three-dimensional instabilities of a spatially periodic shear layer. *J. Fluid Mech.* **114**, 59.
- PRADEEP, D. S. 1999 Core dynamics of a strained vortex column: linear instability, nonlinear evolution, and transition. MS Thesis, University of Houston.
- ROBINSON, A. C. & SAFFMAN, P. G. 1984 Three-dimensional stability of an elliptical vortex in a straining field. *J. Fluid Mech.* **142**, 451.
- ROGERS, M. M. & MOSER, R. D. 1992 The three-dimensional evolution of a plane mixing layer: the Kelvin-Helmholtz rollup. *J. Fluid Mech.* **243**, 183.
- SAFFMAN, P. G. 1992 *Vortex Dynamics*. Cambridge University Press.
- SAMUELS, D. C. 1998 A finite-length instability of vortex tubes. *Eur. J. Mech. B/Fluids* **17**, 587.
- SCHOPPA, W., HUSSAIN, F. & METCALFE, R. W. 1995 A new mechanism of small-scale transition in a plane mixing layer: core dynamics of spanwise vortices. *J. Fluid Mech.* **298**, 23.
- SIPP, D. & JACQUIN, L. 1998 Elliptic instability in two-dimensional flattened Taylor-Green vortices. *Phys. Fluids* **10**, 839.
- SIPP, D., LAUGA, E. & JACQUIN, L. 1999 Vortices in rotating systems: Centrifugal, elliptic and hyperbolic instabilities. *Phys. Fluids* **11**, 3716.

- STANAWAY, S., SHARIFF, K. & HUSSAIN, F. 1988 Head-on collision of viscous vortex rings. *CTR Rep.* S-88, p. 287.
- STUART, J. T. 1967 On finite amplitude oscillations in laminar mixing layers. *J. Fluid Mech.* **29**, 417.
- TSAI, C.-Y. & WIDNALL, S. E. 1976 The stability of short waves on a straight vortex filament in a weak externally imposed strain field. *J. Fluid Mech.* **73**, 721.
- VERZICCO, R. & JIMÉNEZ, J. 1999 On the survival of strong vortex filaments in 'model' turbulence. *J. Fluid Mech.* **394**, 261.
- VERZICCO, R., JIMÉNEZ, J. & ORLANDI, P. 1995 On steady columnar vortices under local compression. *J. Fluid Mech.* **299**, 367.
- VINCENT, A. & MENEGUZZI, M. 1994 On the dynamics of vorticity tubes in homogeneous turbulence. *J. Fluid Mech.* **258**, 245.
- VIRK, D., HUSSAIN, F. & KERR, R. M. 1995 Compressible vortex reconnection. *J. Fluid Mech.* **304**, 47.
- WALEFFE, F. 1990 On the three-dimensional instability of strained vortices. *Phys. Fluids A* **2**, 76.